



**HAL**  
open science

## Control of Ca<sup>2+</sup> signals by astrocyte nanoscale morphology at tripartite synapses

Audrey Denizot, Misa Arizono, Valentin Nägerl, Hugues Berry, Erik de Schutter

► **To cite this version:**

Audrey Denizot, Misa Arizono, Valentin Nägerl, Hugues Berry, Erik de Schutter. Control of Ca<sup>2+</sup> signals by astrocyte nanoscale morphology at tripartite synapses. *Glia*, 2022, 10.1002/glia.24258. hal-03582629v2

**HAL Id: hal-03582629**

**<https://inria.hal.science/hal-03582629v2>**






Submitted on 12 Oct 2022

**HAL** is a multi-disciplinary open access archive for the deposit and dissemination of scientific research documents, whether they are published or not. The documents may come from teaching and research institutions in France or abroad, or from public or private research centers.

L'archive ouverte pluridisciplinaire **HAL**, est destinée au dépôt et à la diffusion de documents scientifiques de niveau recherche, publiés ou non, émanant des établissements d'enseignement et de recherche français ou étrangers, des laboratoires publics ou privés.

## RESEARCH ARTICLE

# Control of Ca<sup>2+</sup> signals by astrocyte nanoscale morphology at tripartite synapses

Audrey Denizot<sup>1</sup>  | Misa Arizono<sup>2,3,4</sup>  | U. Valentin Nägerl<sup>2,3</sup>  |  
Hugues Berry<sup>5,6</sup>  | Erik De Schutter<sup>1</sup> <sup>1</sup>Computational Neuroscience Unit, Okinawa Institute of Science and Technology, Onna-Son, Japan<sup>2</sup>Interdisciplinary Institute for Neuroscience, Université de Bordeaux, Bordeaux, France<sup>3</sup>Interdisciplinary Institute for Neuroscience, CNRS UMR 5297, Bordeaux, France<sup>4</sup>Department of Pharmacology, Kyoto University Graduate School of Medicine, Kyoto, Japan<sup>5</sup>LIRIS, UMR5205 CNRS, Univ Lyon, Villeurbanne, France<sup>6</sup>INRIA, Villeurbanne, France**Correspondence**

Audrey Denizot, Okinawa Institute of Science and Technology, Computational Neuroscience Unit, Onna-Son, Japan.

Email: [audrey.denizot3@oist.jp](mailto:audrey.denizot3@oist.jp)**Funding information**

Japan Society for the Promotion of Science, Grant/Award Number: P21733; Okinawa Institute of Science and Technology Graduate University; European Research Council Synergy grant (ENSEMBLE), Grant/Award Number: 951294

**Abstract**

Much of the Ca<sup>2+</sup> activity in astrocytes is spatially restricted to microdomains and occurs in fine processes that form a complex anatomical meshwork, the so-called spongiform domain. A growing body of literature indicates that those astrocytic Ca<sup>2+</sup> signals can influence the activity of neuronal synapses and thus tune the flow of information through neuronal circuits. Because of technical difficulties in accessing the small spatial scale involved, the role of astrocyte morphology on Ca<sup>2+</sup> microdomain activity remains poorly understood. Here, we use computational tools and idealized 3D geometries of fine processes based on recent super-resolution microscopy data to investigate the mechanistic link between astrocytic nanoscale morphology and local Ca<sup>2+</sup> activity. Simulations demonstrate that the nano-morphology of astrocytic processes powerfully shapes the spatio-temporal properties of Ca<sup>2+</sup> signals and promotes local Ca<sup>2+</sup> activity. The model predicts that this effect is attenuated upon astrocytic swelling, hallmark of brain diseases, which we confirm experimentally in hypo-osmotic conditions. Upon repeated neurotransmitter release events, the model predicts that swelling hinders astrocytic signal propagation. Overall, this study highlights the influence of the complex morphology of astrocytes at the nanoscale and its remodeling in pathological conditions on neuron-astrocyte communication at so-called tripartite synapses, where astrocytic processes come into close contact with pre- and postsynaptic structures.

**KEYWORDS**

calcium microdomains, computational neuroscience, intracellular signaling, nano-morphology, reaction-diffusion simulations

## 1 | INTRODUCTION

Astrocytes are glial cells of the central nervous system that are essential for brain development and function (Verkhratsky and Nedergaard 2018). They notably modulate neuronal communication at synapses. Astrocytic Ca<sup>2+</sup> signals are triggered by neurotransmitters released by

active neurons, which can trigger the release of neuroactive molecules by the astrocyte, referred to as gliotransmitters. The first type of astrocytic Ca<sup>2+</sup> signals that has been observed was Ca<sup>2+</sup> waves that propagate through gap junctions in astrocyte networks (Giaume and Venance 1998). Ca<sup>2+</sup> waves have also been observed in the branches of single astrocytes, sporadically propagating to the soma

This is an open access article under the terms of the [Creative Commons Attribution-NonCommercial](https://creativecommons.org/licenses/by-nc/4.0/) License, which permits use, distribution and reproduction in any medium, provided the original work is properly cited and is not used for commercial purposes.

© 2022 The Authors. *GLIA* published by Wiley Periodicals LLC.

(Haustein et al. 2014; Bindocci et al. 2017). The recent development of  $\text{Ca}^{2+}$  imaging techniques with improved spatial and temporal resolution has revealed the existence of spatially-restricted  $\text{Ca}^{2+}$  signals in astrocytes, referred to as microdomains or hotspots (Di Castro et al. 2011; Panatier et al. 2011; Stobart, Ferrari, Barrett, Glück, et al. 2018; Srinivasan et al. 2015; Shigetomi et al. 2013; Sherwood et al. 2017; Otsu et al. 2015; Lind et al. 2013; Bindocci et al. 2017; Agarwal et al. 2017; Arizono et al. 2020; Otsu et al. 2015; Grosche et al. 1999). These local  $\text{Ca}^{2+}$  signals account for the vast majority ( $\approx 80\%$ ) of astrocytic  $\text{Ca}^{2+}$  activity and occur in fine processes, which occupy 75% of the astrocytic volume (Bindocci et al. 2017), forming the spongiform domain, also referred to as the gliapil. Given that one astrocyte may contact tens of thousands of synapses simultaneously (Bushong et al. 2002) via these fine processes, local and fast  $\text{Ca}^{2+}$  signals might enable the astrocyte to powerfully yet precisely control the flow of information through synaptic circuits. Importantly, reactive astrocytes, hallmark of brain diseases, display aberrant amplitude, duration, frequency and spatial spread of  $\text{Ca}^{2+}$  signals (Shigetomi et al. 2019; Nedergaard et al. 2010; Lee et al. 2022).

Cellular micro-morphology lends itself to the compartmentalization of biochemical signals. For example, the anatomical design of dendritic spines restricts the diffusion of  $\text{Ca}^{2+}$  to the activated synapse, which reduces cross-talk between nearby synapses (Santamaria et al. 2011; Tonnesen et al. 2014; Yuste et al. 2000; Noguchi et al. 2005; Yasuda 2017; Holcman and Schuss 2011). The complex shapes of Bergmann glia (Grosche et al. 1999) and perisynaptic “astrocytic compartments” along major branches (Panatier et al. 2011) have been proposed to restrict  $\text{Ca}^{2+}$  signals to the vicinity of synapses. Fine processes of the spongiform domain, however, cannot be resolved by diffraction-limited light microscopy (Rusakov 2015), so that the contribution of their morphology to shaping local  $\text{Ca}^{2+}$  signals is poorly understood. Our recent 3D STED study (Arizono et al. 2020) revealed the structural basis of compartmentalized spontaneous  $\text{Ca}^{2+}$  signals in fine astrocytic processes. Importantly, pathological changes in astrocytic morphology (Lafrenaye and Simard 2019), such as “astrocytic swelling,” are paired with aberrant  $\text{Ca}^{2+}$  signals (Shigetomi et al. 2019). We have recently reported that swelling can also occur at the level of fine astrocytic processes (Arizono, Bancelin, et al. 2021). The effect of such a remodeling of astrocytic nano-morphology on the local  $\text{Ca}^{2+}$  signals involved in regulating synapses remains yet unclear. Together, there is a great interest in understanding the mechanistic link between the nano-morphology of astrocytic processes and  $\text{Ca}^{2+}$  profiles in health and disease. Computational approaches make it possible to simulate different geometrical scenarios, in a much more systematic and controlled way than what could be done experimentally. Computational models can thus help us gain insights into the impact of morphological parameters on  $\text{Ca}^{2+}$  activity.

Here, we use computational tools to explore the role of the anatomical design of the gliapil. To do so, we perform simulations in branchlet geometries that we designed based on super-resolution microscopy data reported in live tissue (Arizono et al. 2020), consisting of nodes, which host  $\text{Ca}^{2+}$  microdomains, and their intervening shafts of variable widths. Our simulation results suggest that the

nanoscale design of the spongiform domain effectively decreases diffusion flux, which increases  $\text{Ca}^{2+}$  peak probability, duration and amplitude in the stimulated and neighboring nodes. To test those predictions, we performed  $\text{Ca}^{2+}$  recordings in organotypic hippocampal cultures in hypo-osmotic conditions, where the normal node-shaft arrangement is altered. In line with our model predictions,  $\text{Ca}^{2+}$  activity in hypo-osmotic conditions was decreased compared to  $\text{Ca}^{2+}$  activity in normal tissue. We further found that, upon repeated neuronal stimulation, thin shafts allow signal propagation even if some stimuli are omitted, thus allowing for a more robust signal propagation.

Overall, our study sheds light on the influence of the nanoscale morphology of the complex spongiform domain of astrocytes on  $\text{Ca}^{2+}$  microdomain activity and indicates that pathological morphological changes may substantially affect their  $\text{Ca}^{2+}$  activity.

## 2 | METHODS

### 2.1 | Stochastic spatially-explicit voxel-based simulations

In order to model astrocyte  $\text{Ca}^{2+}$  signals in astrocyte branchlets, we have used the voxel-based “GCaMP” implementation of the Inositol 3-Phosphate ( $\text{IP}_3$ ) receptor-dependent  $\text{Ca}^{2+}$  signaling model from Denizot et al. (2019), using the same reaction scheme and parameter values (Figure 1b). Briefly, we model  $\text{Ca}^{2+}$  fluxes in and out of the cytosol, mediated by  $\text{Ca}^{2+}$  channels and pumps on the endoplasmic reticulum (ER) and on the plasma membrane.  $\text{Ca}^{2+}$  signals occur when some  $\text{IP}_3$ R channels are in the open state.  $\text{IP}_3$  can be synthesized by the  $\text{Ca}^{2+}$ -dependent activity of phospholipase  $\text{C}\delta$  ( $\text{PLC}\delta$ ) and the removal of  $\text{IP}_3$  molecules from the cytosol is expressed as a single decay rate.  $\text{IP}_3$ R kinetics is described by a Markov model, derived from De Young & Keizer’s model (De Young and Keizer 1992). Each  $\text{IP}_3$ R molecule contains one  $\text{IP}_3$  binding site and two  $\text{Ca}^{2+}$  binding sites. An  $\text{IP}_3$ R is in the open state when in state  $\{110\}$  (first Ca site and  $\text{IP}_3$  bound, second Ca site free). Depending on the simulation, other diffusing molecules were added to the model, such as the fluorescent molecule ZsGreen and fluorescent  $\text{Ca}^{2+}$  indicators, here 10  $\mu\text{M}$  of GCaMP6s. GCaMPs are genetically-encoded  $\text{Ca}^{2+}$  indicators (GECIs) that are derived from the fluorescent protein GFP and the  $\text{Ca}^{2+}$  buffer calmodulin (see Shigetomi et al. (2016) for a review on GECIs). Unless specified otherwise, simulation time  $T$  was 50s. Data collection interval was 1 ms. For further details on the kinetic scheme and model assumptions, please refer to Denizot et al. (2019).

The model was implemented using the STochastic Engine for Pathway Simulation (STEPS, <http://steps.sourceforge.net/>), a python package performing exact stochastic simulation of reaction-diffusion systems (Hepburn et al. 2012). More precisely, simulations were performed using the spatial stochastic “Tetexact” solver, based on Gillespie’s Stochastic Simulation Algorithm (SSA) (Gillespie 1977), extended for diffusive fluxes across voxels in tetrahedral meshes (Hepburn et al. 2012). Diffusion is treated as a first order reaction in the SSA system,

whose rate is determined by the diffusion coefficient of the diffusing species.

Simulations in STEPS can be performed in complex geometries in three spatial dimensions. Space is divided into well-mixed tetrahedral compartments, referred to as voxels. Reactions between two molecules can only occur if they are located within the same voxel. Diffusion events are modeled as a decrease of the number of molecules in the original voxel and an increase in the number of molecules in its neighboring voxel. Boundary conditions, except when specified otherwise, were reflective. In other words, mobile molecules could not diffuse away from the geometry, as if they were “bouncing” onto the plasma membrane. STEPS enables to compute, in complex 3D geometries, reactions and diffusion in the cytosol as well as reactions between cytosolic molecules and molecules located at the plasma or ER membrane.

## 2.2 | Geometries

Typical astrocyte branchlet geometries were designed from their recent experimental characterization in live tissue at high spatial resolution (50 nm in x-y) (Arizono et al. 2020). Those geometries consist in alternations of bulbous structures, nodes, connected to each other with cylindrical structures, shafts. Geometries with different shaft widths  $d_{\text{shaft}}$  were designed using Trelis software (<https://www.csimsoft.com/trelis>, Figure 1a). The geometry of a node was approximated as being a sphere of diameter 380 nm. Shaft geometry consisted in a 1  $\mu\text{m}$  long cylinder. Shaft diameter was defined relative to node diameter. For example, shaft diameter was the same as node diameter, that is,  $d_{\text{shaft}} = d_0 = 380$  nm. Similarly, shaft diameter was 190 nm and 127 nm for  $d_{\text{shaft}} = \frac{d_0}{2}$  and  $\frac{d_0}{3}$ , respectively. Cones were positioned between spheres and cylinders in order to create a smoother transition between nodes and shafts, better approximating the geometry observed experimentally. Cytosolic volume was thus  $V_1 = 0.620 \mu\text{m}^3$ ,  $V_2 = 0.263 \mu\text{m}^3$ , and  $V_3 = 0.195 \mu\text{m}^3$ , for  $d_{\text{shaft}} = d_0$ ,  $\frac{d_0}{2}$  and  $\frac{d_0}{3}$ , respectively. Please note that molecular concentrations were the same in all simulations, so that the total number of molecules in basal conditions in shafts varied depending on shaft width. A subset of simulations was performed in a geometry with  $V_1 = 0.258 \mu\text{m}^3$ . This geometry is characterized, similarly to geometries with  $d_{\text{shaft}} = d_0$ , by a node/shaft width ratio of 1. It contains cylinders of length 750 nm, diameter 285 nm and spheres of diameter 285 nm. As a first approximation, ER geometry was considered to be similar to the geometry of the astrocyte branchlet: node/shaft successions. ER nodes were aligned with cytosolic nodes. As no quantification of the ratio between astrocytic ER volume and cellular volume was found in the literature, ER volume was 10% of the total branchlet volume, based on available data in neurons (Spacek and Harris 1997). As the shape and distribution of the ER in fine processes have not been characterized in live tissue but are likely highly variable, additional simulations were performed in meshes with various ER shapes: “No ER,” “Node ER,” and “Cyl ER,” in which there was no ER, discontinuous ER in nodes or cylindrical ER, respectively (Figures S7–S9). The cytosolic

**TABLE 1** Characteristics of the geometries of astrocyte branchlets used in this study.  $V_{\text{cyt}}$  is the cytosolic volume,  $S_{\text{PM}}$  is the area of the plasma membrane and  $S_{\text{ER}}$  is the area of the ER membrane. Volumes are expressed in  $\text{nm}^3$  and areas in  $\text{nm}^2$ . Meshes are available at <http://modeldb.yale.edu/266928>.

Geometry	$V_{\text{cyt}}$ ( $\text{nm}^3$ )	$S_{\text{PM}}$ ( $\text{nm}^2$ )	$S_{\text{ER}}$ ( $\text{nm}^2$ )
“5nodes” $d_{\text{shaft}} = d_0$	$6.20 \times 10^8$	$7.73 \times 10^6$	$2.19 \times 10^6$
“5nodes” $d_{\text{shaft}} = d_0/2$	$2.63 \times 10^8$	$4.95 \times 10^6$	$1.28 \times 10^6$
“5nodes” $d_{\text{shaft}} = d_0/3$	$1.95 \times 10^8$	$4.10 \times 10^6$	$9.99 \times 10^5$
“No ER” $d_{\text{shaft}} = d_0$	$6.73 \times 10^8$	$7.73 \times 10^6$	0.00
“No ER” $d_{\text{shaft}} = d_0/2$	$2.83 \times 10^8$	$4.95 \times 10^6$	0.00
“No ER” $d_{\text{shaft}} = d_0/3$	$2.10 \times 10^8$	$4.09 \times 10^6$	0.00
“Node ER” $d_{\text{shaft}} = d_0$	$6.67 \times 10^8$	$7.75 \times 10^6$	$4.17 \times 10^5$
“Node ER” $d_{\text{shaft}} = d_0/2$	$2.74 \times 10^8$	$4.96 \times 10^6$	$4.37 \times 10^5$
“Node ER” $d_{\text{shaft}} = d_0/3$	$2.00 \times 10^8$	$4.11 \times 10^6$	$4.41 \times 10^5$
“Cyl ER” $d_{\text{shaft}} = d_0$	$6.27 \times 10^8$	$7.74 \times 10^6$	$2.03 \times 10^6$
“Cyl ER” $d_{\text{shaft}} = d_0/2$	$2.77 \times 10^8$	$4.95 \times 10^6$	$8.78 \times 10^5$
“Cyl ER” $d_{\text{shaft}} = d_0/3$	$2.07 \times 10^8$	$4.09 \times 10^6$	$5.86 \times 10^5$

volume, plasma and ER membrane surface areas of those 3D geometries are presented in Table 1.

A sensitivity study was performed to investigate the effect of voxel size on the kinetics of the molecular interactions modeled. Information on the voxel sizes of the different meshes used is presented in Table S1. Results are presented in Figure S1. Meshes that contained voxels that were  $<50 \text{ nm}^3$  were characterized by aberrant kinetics, resulting in aberrant average numbers of molecules in a given state. Those results thus suggest that to prevent errors due to voxel size, meshes should not display voxel sizes that are  $<50 \text{ nm}^3$ . We have thus made sure, while meshing the geometries in which simulations were ran, that no voxels were  $<50 \text{ nm}^3$ . Minimum voxel size was 443, 1100, and 447  $\text{nm}^3$ , for  $d_{\text{shaft}} = d_0$ ,  $\frac{d_0}{2}$  and  $\frac{d_0}{3}$  geometries, respectively.

In a subset of simulations, ER geometry varied. The shape of the cell was the same as in “5nodes” geometries (Figure 1). ER geometry consisting of node/shaft alternations, described above, is referred to as “Node/shaft ER.” “No ER” geometry contains no ER. “Node ER” is characterized by a discontinuous ER geometry, consisting in spheres of diameter 54 nm, located in cellular nodes. “Cyl ER” corresponds to a cylindrical ER, of length  $l_{\text{ER}} = 6274$  nm and a diameter of 108, 54, and 36 nm, for  $d_{\text{shaft}} = d_0$ ,  $\frac{d_0}{2}$  and  $\frac{d_0}{3}$ , respectively. The associated cytosolic volume, ER and plasma membrane area are presented in Table 1.

## 2.3 | Protocol for simulating bleaching experiments

In order to test whether the idealized geometries presented in Figure 1 are a good approximation of the spongiform ultrastructure of astrocyte branchlets, we have simulated their fluorescence recovery

after photobleaching (FRAP) experiments. Briefly, laser pulses are simulated on a node (region of interest) while the fluorescence level is being recorded. At bleaching time, the fluorescence level in the region of interest decreases to  $I_0$ . Then, because of the diffusion of fluorescent molecules into the region of interest, fluorescence increases until it reaches a new steady state,  $I_{inf}$ . We characterize node compartmentalization by measuring the time  $\tau$  taken by fluorescing molecules to diffuse into the node to reach  $I_{inf}$ . In other words, a high node compartmentalization will be associated with a high value of  $\tau$ . Thus, three main parameters characterize bleaching traces:  $I_0$ ,  $\tau$  and  $I_{inf}$ .

To mimic bleaching experiments in fine branchlets performed by (Arizono et al. 2020), ZsGreen molecules were added to simulation space. After 2 s of simulation, providing the basal level of fluorescence, 60% of ZsGreen molecules were bleached. In order to fit  $I_0$  and  $I_{inf}$  that were measured experimentally, and as bleaching time lasted 10 ms in experiments and 1 ms in simulations, the bleached volume in simulations was adjusted depending on the geometry (see Figure 2a). Bleaching was simulated as a transition from ZsGreen molecules to ZsGreen-bleached molecules, the latter being considered as non-fluorescing molecules. Screenshots of simulations, illustrating the diffusion of ZsGreen and ZsGreen-bleached molecules, are presented in Figure S2b. The number of ZsGreen molecules in the central node was recorded over simulation time and a fit was performed following Equation (1) to determine the values of  $I_0$ ,  $I_{inf}$  and  $\tau$ .

$$I(t) = I_0 - (I_0 - I_{inf})e^{-t/\tau}, \quad (1)$$

where  $I(t)$  is the level of fluorescence measured at time  $t$ . The coefficient of diffusion,  $D_{ZsGreen}$ , and the concentration,  $[ZsGreen]$ , of ZsGreen were adjusted to fit experimental data. Indeed, the amplitude of  $[ZsGreen]$  fluctuations at steady state is inversely proportional to the number of ZsGreen molecules in the geometry. In other words, fluorescence signals are more noisy when  $[ZsGreen]$  is low. Moreover, the autocorrelation of those fluctuations depends on the coefficient of diffusion of ZsGreen,  $D_{ZsGreen}$ . If  $D_{ZsGreen}$  increases, the autocorrelation of Lag, where Lag is the autocorrelation delay, will decrease faster as Lag increases. Comparing the fluctuations of  $[ZsGreen]$  and its autocorrelation in experiments and in simulations thus enabled to find the values of  $D_{ZsGreen}$  and of  $[ZsGreen]$  that allowed for the best fit to experimental data. In the simulations presented here,  $D_{ZsGreen} = 90 \mu\text{m}^2 \cdot \text{s}^{-1}$  and  $[ZsGreen] = 25 \mu\text{M}$ .

## 2.4 | Protocols for simulating neuronal stimulation

In order to investigate the propagation of  $\text{Ca}^{2+}$  signals from nodes that contact neuronal spines, we have developed two different protocols for our simulations, performed in the geometries presented in Figure 1. As nodes were the site of  $\text{Ca}^{2+}$  signal initiation (Arizono et al. 2020) and as most spines contacted nodes rather than shafts, we have simulated neuronal stimulation in nodes. To simulate neuronal stimulation,  $\text{IP}_3$  and  $\text{Ca}^{2+}$  were infused in the cytosol at

stimulation time.  $\text{IP}_3$  infusion reflects the production of  $\text{IP}_3$  by phospholipase C that results from the activation of  $G_q$ -G-protein-coupled receptors (GPCRs).  $\text{Ca}^{2+}$  infusion mimics the influx of  $\text{Ca}^{2+}$  in the cytosol through  $\text{Ca}^{2+}$  channels at the plasma membrane. The rate of this neuronal activity-induced  $\text{Ca}^{2+}$  influx,  $k_{Ca}$ , varied within a physiological range of values, from 0 to  $1000 \text{ s}^{-1}$  (Wu et al. 2018; Brazhe et al. 2018). Signals were recorded both in the stimulated node, Node 1, and in the neighboring node, Node 2.

- In the first protocol, 100  $\text{IP}_3$  molecules were infused in Node 1, at  $t = t_0 = 1 \text{ s}$ , while  $\text{Ca}^{2+}$  activity was monitored in Node 1 and in the neighboring node, Node 2 (see e.g., Figure 3a). Neuronal activity-induced  $\text{Ca}^{2+}$  influx was mediated by generic  $\text{Ca}^{2+}$  channels at the plasma membrane. Twenty-five of those  $\text{Ca}^{2+}$  channels were placed on the plasma membrane of Node 1, corresponding to a similar density to the  $\text{IP}_3\text{R}$  density on the ER membrane, and were set to an inactive state. At stimulation time  $t = t_0$ ,  $\text{Ca}^{2+}$  channels were set to an active state, resulting in an influx of  $\text{Ca}^{2+}$  within the cytosol at rate  $k_{Ca} = 0\text{--}1000 \text{ s}^{-1}$ . At  $t = t_0 + 1$ ,  $\text{Ca}^{2+}$  channels were set back to their initial inactive state. Simulations were performed in geometries with varying shaft width  $d_{\text{shaft}}$ .
- In the second protocol, we have investigated signal propagation in the node/shaft geometry depending on shaft width  $d_{\text{shaft}}$  when several nodes were successively stimulated. In “5 nodes” geometries, 50  $\text{IP}_3$  molecules were infused at  $t_0 = 5 \text{ s}$ ,  $t_0 + \tau_{\text{IP}_3}$ ,  $t_0 + 2\tau_{\text{IP}_3}$ ,  $t_0 + 3\tau_{\text{IP}_3}$  in Nodes 1, 2, 3, and 4, respectively. During the whole simulation time,  $\text{Ca}^{2+}$  activity was recorded in Node 5 (see Figure 5). In a subset of simulations, stimulation of Nodes 2, 3 and 4 occurred with a probability  $1 - p_{\text{fail}}$ , with  $p_{\text{fail}} \in [0, 1]$ .

## 2.5 | Code accessibility

The simulation code, implemented with STEPS 3.5.0, and the meshes are available on ModelDB (McDougal et al. 2017) at <http://modeldb.yale.edu/266928>. The original model from Denizot et al. (2019) is available at <http://modeldb.yale.edu/247694>.

## 2.6 | Peak detection and analysis

The same strategy as developed by Denizot et al. (2019) was used for detecting and analyzing  $\text{Ca}^{2+}$  signals. Briefly, basal concentration of  $\text{Ca}^{2+}$ ,  $[\text{Ca}]_b$ , was defined based on a histogram of the number of  $\text{Ca}^{2+}$  ions in the absence of neuronal stimulation. Peak initiation corresponded to the time when  $[\text{Ca}^{2+}]$  was higher than the following threshold:  $[\text{Ca}]_b + n\sigma_{Ca}$ , where  $\sigma_{Ca}$  is the standard deviation of  $[\text{Ca}^{2+}]$  histogram in the absence of neuronal stimulation. The value of  $n$  was set by hand depending on signal/noise ratio of the simulation of interest. Peak termination corresponded to the time when  $[\text{Ca}^{2+}]$  decreased below the peak threshold.

Several parameters were analyzed to characterize  $\text{Ca}^{2+}$  signals. Peak duration corresponds to the time between peak initiation and

peak termination. Peak amplitude corresponds to the maximum number of  $\text{Ca}^{2+}$  ions recorded in the studied node during peak duration. It is expressed as signal to noise ratio  $\text{SNR} = \frac{A - |C_{a,b}|}{|C_{a,b}|}$ . Time to 1<sup>st</sup> peak corresponds to the delay between the beginning of the simulation and the first peak detection, measured in the cellular compartment of interest. Peak probability corresponds to the fraction of simulations in which at least one peak was detected during simulation time in the region of interest.  $\text{Ca}^{2+}$  residency time was measured by performing  $n = 300$  simulations for each value of  $d_{\text{shaft}}$ , in which only 1  $\text{Ca}^{2+}$  ion was added to node 1, without other molecular species.  $\text{Ca}^{2+}$  residency time corresponds to the time taken by the ion to diffuse away from node 1.

## 2.7 | Organotypic hippocampal slice cultures

All experiments were conducted as described in Arizono et al. (2020) and were in accordance with the European Union and CNRS UMR5297 institutional guidelines for the care and use of laboratory animals (Council directive 2010/63/EU). Organotypic hippocampal slices (Gähwiler type) were dissected from 5 to 7-d-old wild-type mice and cultured 5 to 8 week in a roller drum at 35°C, as previously described (Gähwiler 1981).

## 2.8 | Viral infection

AAV9-GFAP-GCaMP6s (Stobart, Ferrari, Barrett, Stobart, et al. 2018) was injected by brief pressure pulses (40 ms; 15 psi) into the stratum radiatum of 2–3-week old slices from Thy1-YFP-H (JAX:003782) mice 4–6 weeks prior to the experiment.

## 2.9 | Image acquisition

For  $\text{Ca}^{2+}$  imaging, we used a custom-built setup based on an inverted microscope body (Leica DMI6000), as previously described in Tonnesen et al. (2011). We used a 1.3 NA glycerol immersion objective equipped with a correction collar to reduce spherical aberrations and thereby allow imaging deeper inside brain tissue (Urban et al. 2011). The excitation light was provided by a pulsed diode laser ( $\lambda = 485$  nm, PicoQuant, Berlin, Germany). The fluorescence signal was confocally detected by an avalanche photodiode (APD; SPCM-AQRH-14-FC; PerkinElmer). The spatial resolution of the setup was around 200 nm (in  $x$ - $y$ ) and 600 nm ( $z$ ). Confocal time-lapse imaging ( $12.5 \times 25$   $\mu\text{m}$ , pixel size 100 nm) was performed at 2 Hz for 2.5 min in artificial cerebrospinal fluid containing 125 mM NaCl, 2.5 mM KCl, 1.3 mM  $\text{MgCl}_2$ , 2 mM  $\text{CaCl}_2$ , 26 mM  $\text{NaHCO}_3$ , 1.25 mM  $\text{NaH}_2\text{PO}_4$ , 20 mM D-glucose, 1 mM Trolox; 300 mOsm; pH 7.4. Perfusion rate was 2 ml/min and the temperature 32°C. Hypo-osmotic stress (300–200 mOsm) was applied by perfusing ACSF with reduced NaCl concentration (119–69 mM NaCl).

## 2.10 | Image analysis

Image analysis was performed as described in Arizono et al. (2020).  $\text{Ca}^{2+}$  events in the spongiform structure were detected and analyzed using the ImageJ LC\_Pro plugin (Francis et al. 2012), which allows automatic and unbiased detection of  $\text{Ca}^{2+}$  events.

## 2.11 | Experimental design and statistical analysis

For each parameter set, 20 simulations, with different seed values, were generated to get a large enough sample size for statistical analysis while keeping the computational cost of the work to a minimum. Each parameter describing  $\text{Ca}^{2+}$  dynamics was expressed as mean  $\pm$  standard deviation. The effect of  $d_{\text{shaft}}$  on each  $\text{Ca}^{2+}$  signal characteristic was tested using one-way ANOVA. Comparison between two different conditions was performed using unpaired Student *T*-test if values followed a Gaussian distribution, Mann-Whitney test otherwise. Significance is assigned by \* for  $p \leq 0.05$ , \*\* for  $p \leq 0.01$ , \*\*\* for  $p \leq 0.001$ .

## 3 | RESULTS

### 3.1 | Geometrical representation of typical astrocyte processes

In order to investigate the role of the nano-morphology of astrocytic processes on the spatio-temporal properties of  $\text{Ca}^{2+}$  microdomains, we have designed geometries of typical astrocyte processes, derived from our recent characterization of their ultrastructure at a high spatial resolution (50 nm in  $x$ - $y$ ) in organotypic hippocampal culture as well as in acute slices and in vivo (Arizono et al. 2020) (Figure 1a). Geometries consist of alternations of bulbous structures, nodes, connected to each other via cylindrical structures, referred to as shafts. At this spatial scale, cell swelling resulting from hypo-osmotic conditions is not homogeneous: node width is constant while shaft width increases (Figure 3 in Arizono, Inavalli, et al. 2021). To test the effect of such morphological changes of node-shaft structures on astrocytic activity, we designed idealized node-shaft geometries in three spatial dimensions in which we could perform reaction-diffusion simulations of astrocytic calcium signaling. In those geometries, node width was  $d_0 = 380$  nm, consistent with median values of node width reported previously (Arizono et al. 2020). The range of shaft width tested was based on node-shaft width ratios that we measured in organotypic hippocampal culture using STED microscopy (Figure 1a2). The resulting 3D geometries are presented in Figure 1b. To model astrocytic  $\text{Ca}^{2+}$  activity with a high spatial resolution while taking into account the randomness of reactions in small volumes, we used the stochastic voxel-based model from Denizot et al. (2019). The reactions included in the model are presented in Figure 1d and in the Methods section. As the majority of  $\text{Ca}^{2+}$  signals in astrocytes result from the opening of Inositol 3-Phosphate receptors (IP<sub>3</sub>Rs), located at the membrane of the endoplasmic reticulum (ER) (Srinivasan et al. 2015), signals in the

model result from the opening of IP<sub>3</sub> 3Rs, while IP<sub>3</sub> 3R-independent Ca<sup>2+</sup> fluxes into the cytosol are lumped into a single rate  $\gamma$  (see Denizot et al. (2019) for more details on the model's assumptions). Neuronal stimulation was simulated as an injection of IP<sub>3</sub> molecules in the cytosol and a Ca<sup>2+</sup> influx at Ca<sup>2+</sup> channels at the plasma membrane at a rate  $k_{Ca} = 0-1000 \text{ s}^{-1}$ . Astrocytic activity was quantified by measuring Ca<sup>2+</sup> peak probability, frequency, amplitude, duration and time to 1<sup>st</sup> peak (see Figure 1 and Methods).

### 3.2 | Validation of the geometrical model of astrocyte processes

In order to test whether the geometries designed in this study are a good approximation of the ultrastructure of the gliapil, we have compared molecular diffusion flux in those geometries with those reported experimentally. To do so, we simulated photobleaching experiments and compared our results to experimental results from Arizono et al. (2020). The principle of bleaching simulations is presented in the Methods section and in Movie S1. Here, we refer to an increased node compartmentalization when the time to recovery after bleaching,  $\tau$ , increases (see Figure 2b).

Bleaching traces in simulations are both qualitatively (Figure 2b) and quantitatively (Figure 2c) similar to experimental bleaching traces, for shaft width  $d_{\text{shaft}} = d_0$  and  $d_{\text{shaft}} = \frac{d_0}{2}$ . Indeed, no significant difference

of  $I_0$  (Figure 2c1),  $I_{\text{inf}}$  (Figure 2c2) and  $\tau$  (Figure 2c3) was observed between simulations and experimental traces. Simulations were also performed with  $d_{\text{shaft}} = \frac{d_0}{3}$ . Our simulations successfully reproduce experimental bleaching experiments and suggest that  $\tau$ , and thus node compartmentalization, increases when shaft width decreases (Figure 2c3). This result is not surprising as a decreased shaft width results in a smaller size of the exit point for diffusing molecules from the node. This is similar to, for example, dendritic spines, which compartmentalization is increased for thinner spine necks (Santamaria et al. 2011; Tonnesen et al. 2014). The geometries that we have designed can thus be considered as a reasonable approximation of the ultrastructure of the gliapil observed experimentally in live tissue.

### 3.3 | Thin shafts enhance Ca<sup>2+</sup> activity in nodes

About 80% of astrocyte Ca<sup>2+</sup> activity occurs in the gliapil (Bindocci et al. 2017), which suggests that most neuron-astrocyte communication occurs at fine astrocytic processes. As we observed that a decreased shaft width is associated with a decreased diffusion flux, that is, an increased compartmentalization of nodes, we have tested

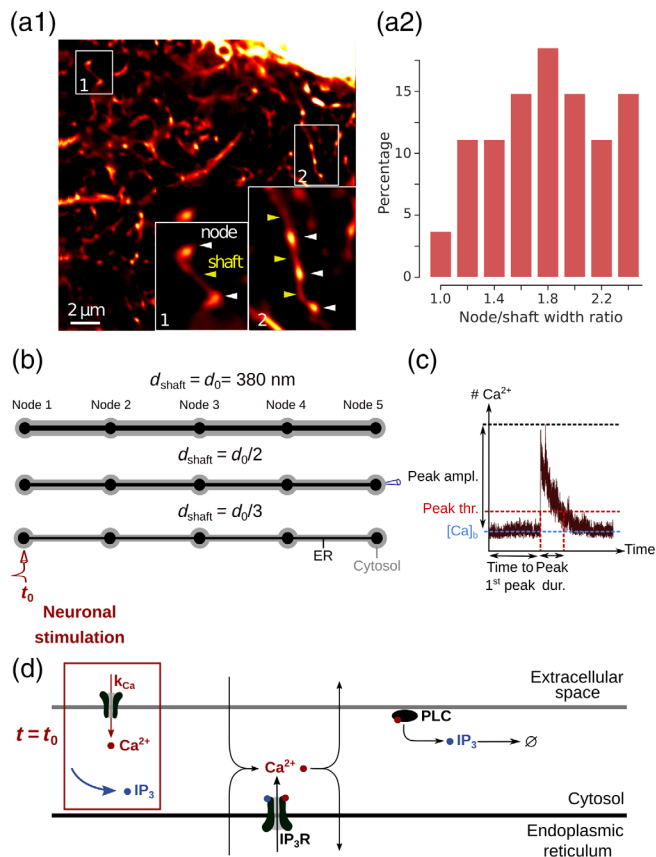


**FIGURE 1** Geometries and kinetic scheme used for simulating Ca<sup>2+</sup> dynamics in node/shaft structures of the gliapil. (a1) Representative STED image showing the astrocytic spongiform domain. Zoom-in images show its anatomical units: Nodes and shafts. (a2) Distribution of the ratio between node width and the width of its neighboring shaft, measured using STED microscopy,  $n = 28$ . (b) Idealized geometries designed to reproduce the node/shaft ultrastructure of the spongiform domain. Nodes are approximated as spheres of diameter 380 nm and shafts as 1  $\mu\text{m}$ -long cylinders, based on their recent characterization in live tissue by Arizono et al. (2020) (Figure 1i–k. Shaft width varied based on experimentally-observed node-shaft width ratios reported in panel b:  $d_{\text{shaft}} = d_0 = 380 \text{ nm}$ ,  $d_{\text{shaft}} = \frac{d_0}{2}$  and  $d_{\text{shaft}} = \frac{d_0}{3}$ . The geometries designed in this study, referred to as “5 nodes,” contain 5 identical nodes and 4 identical shafts. Unless specified otherwise, ER geometry (black) also consists in node/shaft successions (see Methods). The associated cytosolic volume, plasma and ER membrane areas are presented in Table 1. (c) Example of a Ca<sup>2+</sup> trace of the model, recorded in one node. Ca<sup>2+</sup> activity is quantified by measuring time to 1<sup>st</sup> peak, peak probability, amplitude, duration and frequency. A peak is detected when the number of Ca<sup>2+</sup> ions in the recorded node increases above peak threshold  $[Ca]_b + n\sigma_{Ca}$  (see Methods). (d) Biochemical processes included in the model. Ca<sup>2+</sup> can enter/exit the cytosol from/to the extracellular space or the endoplasmic reticulum (ER), resulting from the activity of Ca<sup>2+</sup> channels/pumps. Ca<sup>2+</sup> and IP<sub>3</sub> diffuse in the cytosol following Brownian motion. The kinetics of IP<sub>3</sub>R channels corresponds to the 8-state Markov model from Denizot et al. (2019), adapted from De Young and Keizer (1992); Bezprozvanny et al. (1991). When both IP<sub>3</sub> and Ca<sup>2+</sup> are bound to IP<sub>3</sub>R activating binding sites, the IP<sub>3</sub>R is in open state and Ca<sup>2+</sup> enters the cytosol. Ca<sup>2+</sup> can activate phospholipase C  $\delta$  (PLC $\delta$ ), which results in the production of IP<sub>3</sub>. For more details, please refer to Denizot et al. (2019). Neuronal stimulation is simulated as an infusion of IP<sub>3</sub> in the cytosol and the opening of Ca<sup>2+</sup> channels at the plasma membrane with an influx rate  $k_{Ca}$  (see Methods).

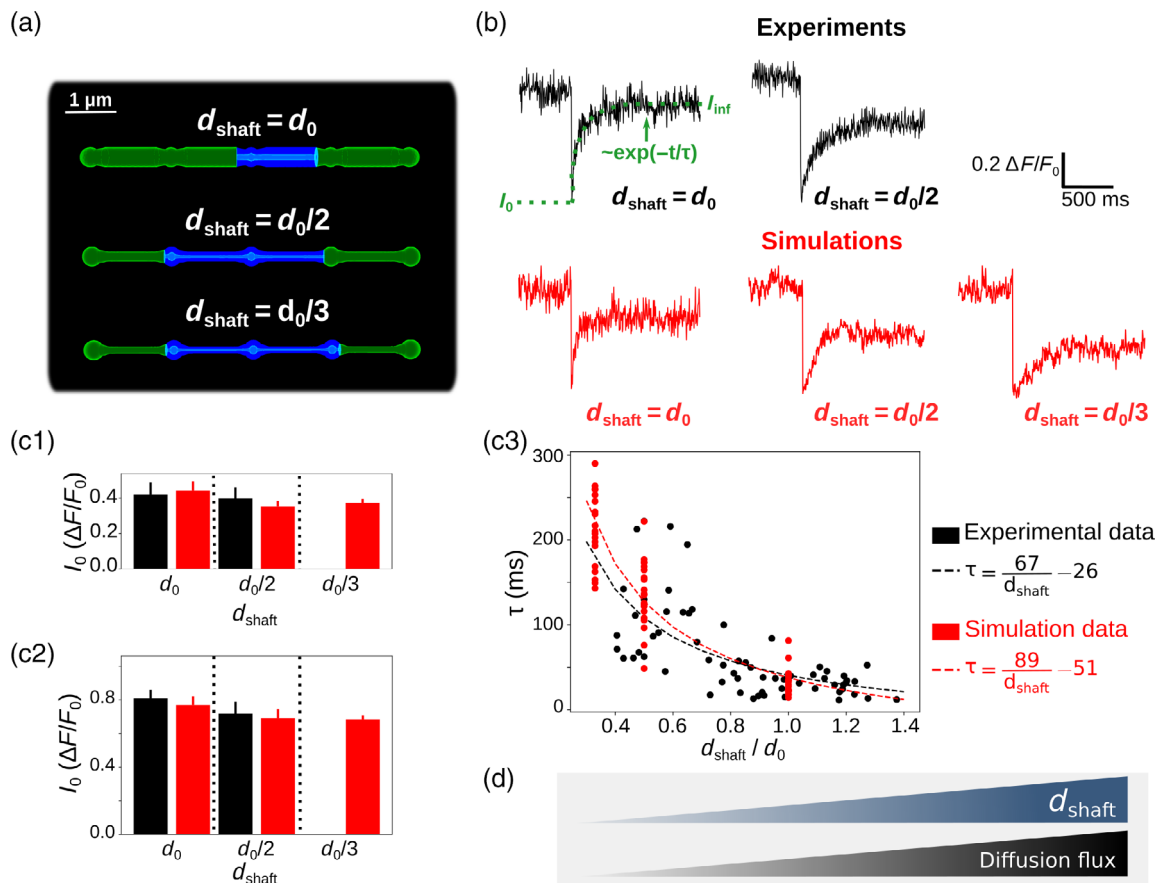


**FIGURE 2** Simulations confirm that thin shafts favor node compartmentalization. (a) Geometries of different shaft widths  $d_{\text{shaft}}$ ,  $d_{\text{shaft}} = d_0$ ,  $\frac{d_0}{2}$  and  $\frac{d_0}{3}$ , used in the bleaching simulations. Blue color represents the bleached volume, which varied depending on the value of  $d_{\text{shaft}}$  in order to fit experimental values of  $I_0$  and  $I_{\text{inf}}$ . (b) Representative experimental (top) and simulation (bottom) traces for different shaft width values.  $I_0$ ,  $I_{\text{inf}}$  and  $\tau$  were calculated using Equation (1). Note that simulations were also performed for  $d_{\text{shaft}} = \frac{d_0}{3}$ . (c) Quantification of  $I_0$  (c1),  $I_{\text{inf}}$  (c2), and  $\tau$  (c3) values in simulations (red) compared to experiments (black). Note that no experimental data was available for  $d_{\text{shaft}} = \frac{d_0}{3}$ . In c1 and c2,  $n = 5 \times 2$  and  $20 \times 3$  for experiments and simulations, respectively. Data are presented as mean  $\pm$  STD. In c3,  $n = 66$  and  $n = 20 \times 3$  for experiments and simulations, respectively.  $\tau$  is negatively correlated to  $d_{\text{shaft}}$  in experiments ( $n = 66$  from 7 slices; Spearman  $r = -0.72$ ,  $p < 0.001^{***}$ ) and simulations ( $n = 60$ ; Spearman  $r = -0.89$ ,  $p < 0.001^{***}$ ). Black and red lines represent curve fit of  $\tau$  as a function of  $d_{\text{shaft}}$  of the form  $\tau = a \cdot \frac{1}{d_{\text{shaft}}} + b$  for experiments and simulations, respectively. (d) Schematic summarizing the conclusion of this figure: Diffusion flux increases with  $d_{\text{shaft}}$ . In that sense, thin shafts favor node compartmentalization. Data in panels c1 and c2 are represented as mean  $\pm$  STD,  $n = 20$  for each geometry.

whether this effect influences  $\text{Ca}^{2+}$  activity upon neuronal stimulation. To do so, we have first analyzed  $\text{Ca}^{2+}$  signals resulting from a single neuronal stimulation, which was simulated as an infusion of  $\text{IP}_3$  and  $\text{Ca}^{2+}$  in the stimulated node, node 1 (see Methods). Those parameters encompass the  $\text{IP}_3$  production by phospholipase C following the activation of  $G_q$ -G-protein-coupled receptors (GPCRs) resulting from the binding of neuronal glutamate, ATP and noradrenaline to  $G_q$  proteins, and  $\text{Ca}^{2+}$  entry at the plasma membrane through  $\text{Ca}^{2+}$  channels, ionotropic receptors or the sodium/calcium exchanger (NCX) functioning in reverse mode (Ahmadpour et al. 2021; Semyanov et al. 2020). Signals were recorded both in the stimulated node, node 1, and in the neighboring node, node 2 (Movie S2). Representative  $\text{Ca}^{2+}$  traces in node 2 for  $d_{\text{shaft}} = d_0$ ,  $\frac{d_0}{2}$  and  $\frac{d_0}{3}$  are displayed in Figure 3a. Our first result is that  $\text{Ca}^{2+}$  peak probability increases when  $d_{\text{shaft}}$  decreases (Figure 3b1). The time to 1<sup>st</sup> peak increases with  $d_{\text{shaft}}$  (Figure 3b2). By contrast, peak amplitude (Figure 3b3) and duration

(Figure 3b4) increase when  $d_{\text{shaft}}$  decreases. Interestingly, time to 1<sup>st</sup> peak was similar in the stimulated and neighboring node, which probably results from the homogenization of  $\text{IP}_3$  concentration throughout the branchlet by diffusion prior to peak detection. To better understand the mechanisms responsible for the increased  $\text{Ca}^{2+}$  peak probability, amplitude and duration when  $d_{\text{shaft}}$  decreases, we measured the frequency of  $\text{IP}_3\text{R}$  opening in nodes 1 and 2. The frequency of  $\text{IP}_3\text{R}$  opening increases when  $d_{\text{shaft}}$  decreases (Figure 3b5). Note that the duration of  $\text{IP}_3\text{R}$  opening and the number of  $\text{IP}_3\text{R}$  s open per  $\text{Ca}^{2+}$  peak did not vary with  $d_{\text{shaft}}$ . The increased  $\text{IP}_3\text{R}$  opening frequency associated with small values of  $d_{\text{shaft}}$  probably results from the increased residency time of molecules in nodes connected to thin shafts (Figure 3c). Indeed, a thin shaft can “trap”  $\text{Ca}^{2+}$  and  $\text{IP}_3$  longer in the node, thus locally increasing the probability of  $\text{IP}_3\text{R}$ s to open, resulting in larger  $\text{Ca}^{2+}$  peaks. For more details, the reader can refer to the theoretical work investigating the narrow escape problem for



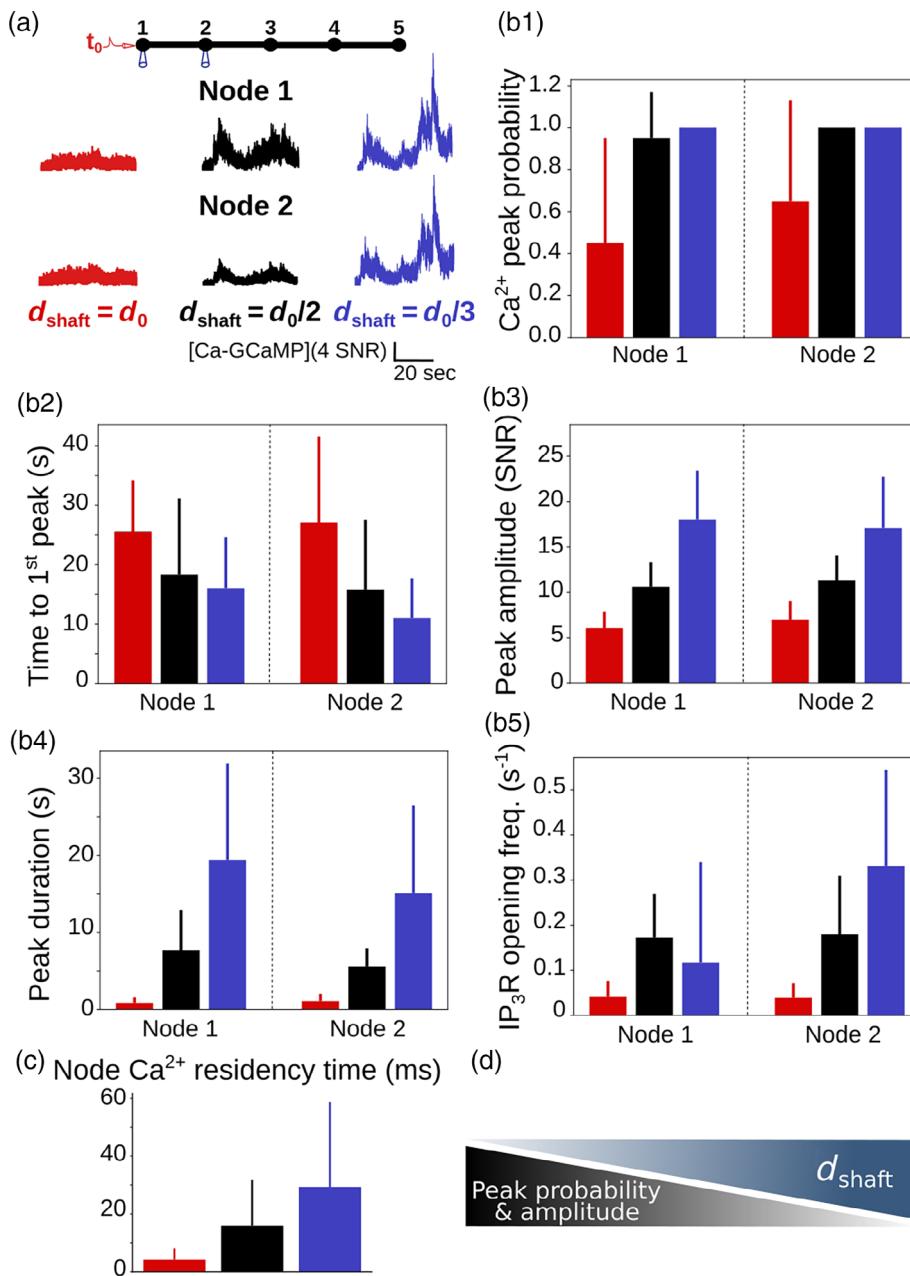


**FIGURE 3**  $\text{Ca}^{2+}$  peak probability, amplitude and duration increase when shaft width decreases. (a) (top) Neuronal stimulation protocol simulated for each geometry: Node 1 was stimulated at  $t = t_0 = 1$  s, while  $\text{Ca}^{2+}$  activity was monitored in node 2. Representative  $\text{Ca}^{2+}$  traces for shaft width  $d_{\text{shaft}} = d_0$  (red),  $d_0/2$  (black) and  $d_0/3$  (blue), expressed as SNR (see Methods). (b) Quantification of the effect of  $d_{\text{shaft}}$  on  $\text{Ca}^{2+}$  signal characteristics data are represented as mean  $\pm$  STD,  $n = 20$ .  $\text{Ca}^{2+}$  peak probability increases (\*\*\*, b1), time to 1<sup>st</sup> peak decreases (\*\*\*, b2), peak amplitude (\*\*\*, b3) and duration (\*\*\*, b4) increase when  $d_{\text{shaft}}$  decreases. (c)  $\text{Ca}^{2+}$  residency time in node 1 increases when  $d_{\text{shaft}}$  decreases (\*\*\*,  $n = 300$ ). (d) Schematic summarizing the main result from this figure:  $\text{Ca}^{2+}$  peak probability and amplitude increase when shaft width decreases.

diffusion in microdomains (Schuss et al. 2007). Nodes connected to thinner shafts, despite being characterized by a lower diffusion flux (Figure 2), could thus consist of signal amplification units, favoring the generation of larger signals, therefore increasing  $\text{Ca}^{2+}$  peak probability, amplitude and duration both in the stimulated and in neighboring nodes.

To identify the cause of the increased  $\text{Ca}^{2+}$  activity when shaft width decreases (Figure 3), we performed simulations in which we altered the stimulated node (Figure 3S2D-E),  $\text{Ca}^{2+}$  influx at the plasma membrane (Figure S3) and boundary conditions (Figure S4). Those parameters did not affect the observed effects of  $d_{\text{shaft}}$  on  $\text{Ca}^{2+}$  dynamics. Furthermore, we repeated simulations of Figure 3 with constant cytosolic volume and constant number of IP<sub>3</sub>Rs, irrespective of the value of  $d_{\text{shaft}}$  (Figure S5). Our results highlight that the relevant

parameter responsible for the observed effects of  $d_{\text{shaft}}$  on  $\text{Ca}^{2+}$  signal characteristics is the node/shaft width ratio or the cytosolic volume rather than  $d_{\text{shaft}}$  itself. Spontaneous  $\text{Ca}^{2+}$  signals were affected by shaft width in the same way as neuronal-induced  $\text{Ca}^{2+}$  signals (Figure S6) and, in particular, reproduced the increase of the amplitude ratio of spontaneous  $\text{Ca}^{2+}$  signals between node 2 and node 1 with shaft width observed in hippocampal organotypic cultures (Arizono et al. 2020). Note that ER morphology, in particular ER surface area (Figures S7, S8 and S9), and  $\text{Ca}^{2+}$  buffering by  $\text{Ca}^{2+}$  indicators (Figure S10), consistent with previous reports (Denizot et al. 2019; Bartol et al. 2015; Majewska et al. 2000), also altered local  $\text{Ca}^{2+}$  activity. Overall, our results suggest that a decreased shaft width, resulting in a decreased diffusion efflux from nodes, increases  $\text{Ca}^{2+}$  peak probability, amplitude and duration. Conversely, the swelling of fine

processes, resulting in an increase of shaft width, attenuates local  $\text{Ca}^{2+}$  peak probability, amplitude, and duration.

### 3.4 | $\text{Ca}^{2+}$ imaging confirms that swelling attenuates local spontaneous $\text{Ca}^{2+}$ activity

To validate the role of thin shafts suggested by our model's predictions, we tried to recreate the widening of shaft width in experimental conditions. Coincidentally, our recent super-resolution study revealed that the nano-architecture of fine processes is remodeled in hypo-osmotic conditions, where shaft width increased while node width remained unaltered (see Figure 3 in Arizono, Inavalli, et al. (2021)). While hypo-osmotic conditions undoubtedly cause many physiological changes to astrocytes, it is the closest experimentally available model to test our model predictions. We thus performed experimental measurements of  $\text{Ca}^{2+}$  activity in fine astrocytic processes under basal and

hypo-osmotic conditions. To record  $\text{Ca}^{2+}$  signals in fine branchlets, we used confocal microscopy in organotypic cultures, which provide a high level of optical access and sample stability in live tissue (resolution  $\approx 200$  nm in x-y versus  $\approx 500$  nm for two-photon microscopy). In accordance with our model's predictions,  $\text{Ca}^{2+}$  peak amplitude and duration were lower in hypo-osmotic compared to basal conditions (Figure 4a-d). Such differences were not observed in the absence of HOC (Figure 4e, f). Overall, our experimental results confirm that the complex nano-architecture of fine astrocytic processes and its alteration, such as cell swelling, shapes local  $\text{Ca}^{2+}$  activity.

### 3.5 | Thin shafts favor more robust signal propagation

As a single branchlet communicates with multiple dendritic spines, which can function independently or belong to a cluster of co-active

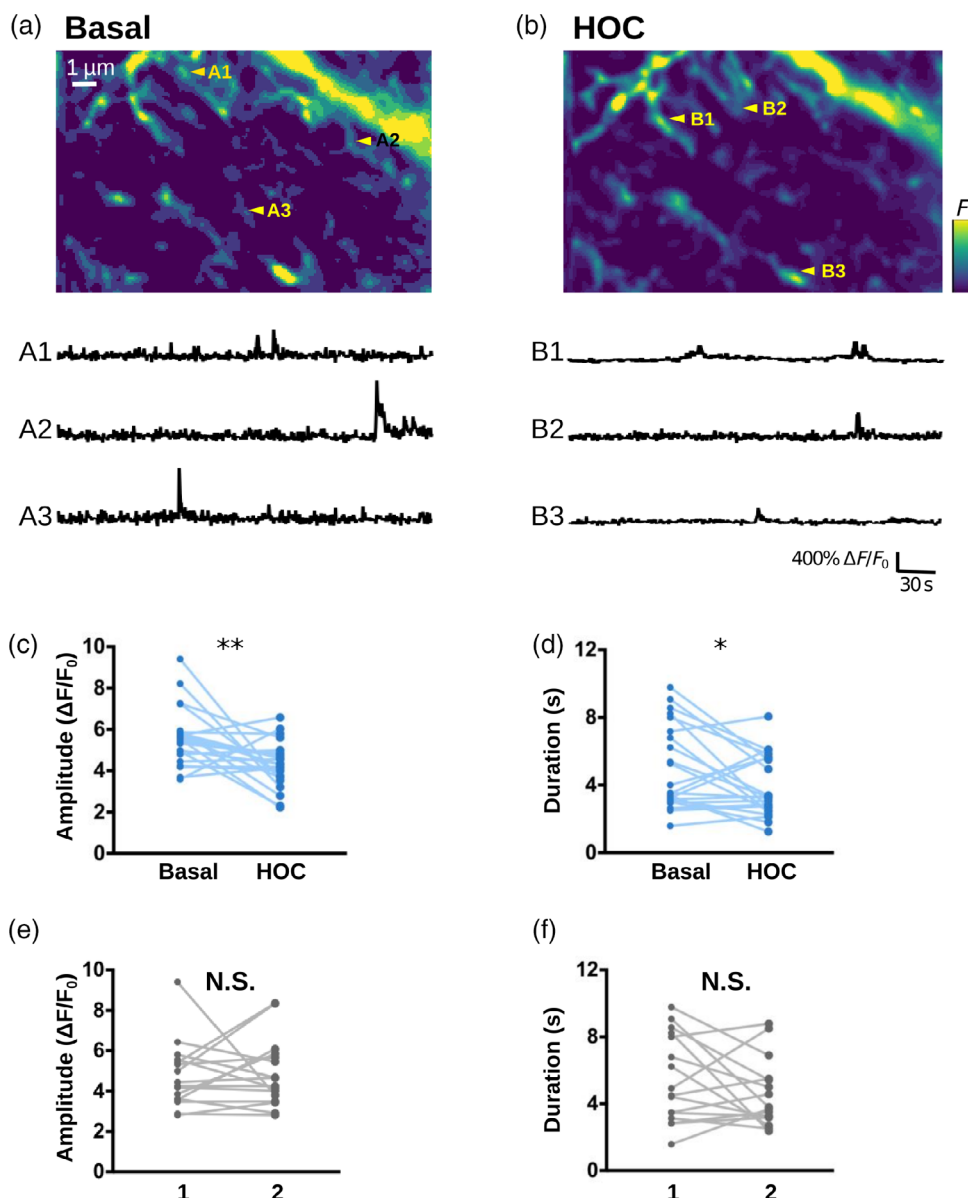


**FIGURE 4**  $\text{Ca}^{2+}$  imaging confirms that swelling attenuates local spontaneous  $\text{Ca}^{2+}$  activity. (a, b) (top) Confocal images of the astrocytic spongiform domain expressing GCaMP6s at baseline (basal, a) and in hypo-osmotic condition (HOC, b), measured in organotypic hippocampal cultures (resolution: 200 nm in x-y, 600 nm in z). (bottom) representative traces of spontaneous  $\text{Ca}^{2+}$  events from ROIs indicated in (a) (a1-a3) and (b) (b1-b3). (c, d)  $\text{Ca}^{2+}$  peak amplitude (c) and duration (d) of spontaneous  $\text{Ca}^{2+}$  events are significantly smaller in hypo-osmotic conditions (HOC) compared to basal conditions (Basal). (e, f) Amplitude (e) and duration (f) of spontaneous  $\text{Ca}^{2+}$  events do not significantly vary when measured twice in a row (1, 2) in the absence of HOC. Lines represent measurements in the same cell, before and after applying hypo-osmotic stress.

synapses (Arizono et al. 2020; Reichenbach et al. 2010; Witcher et al. 2007; Cali et al. 2019; Semyanov et al. 2020), the frequency of node stimulation within the branchlet can vary drastically. Thus, we have tested how node stimulation frequency affects  $\text{Ca}^{2+}$  activity in the

branchlet. To do so, we have performed simulations in which neighboring nodes were repeatedly stimulated after a time period  $\tau_{\text{IP3}}$ , that varied from 50 ms to 5 s, while  $\text{Ca}^{2+}$  signals were recorded in a remote node, node 5 (Figure 5a). In this stimulation protocol, node

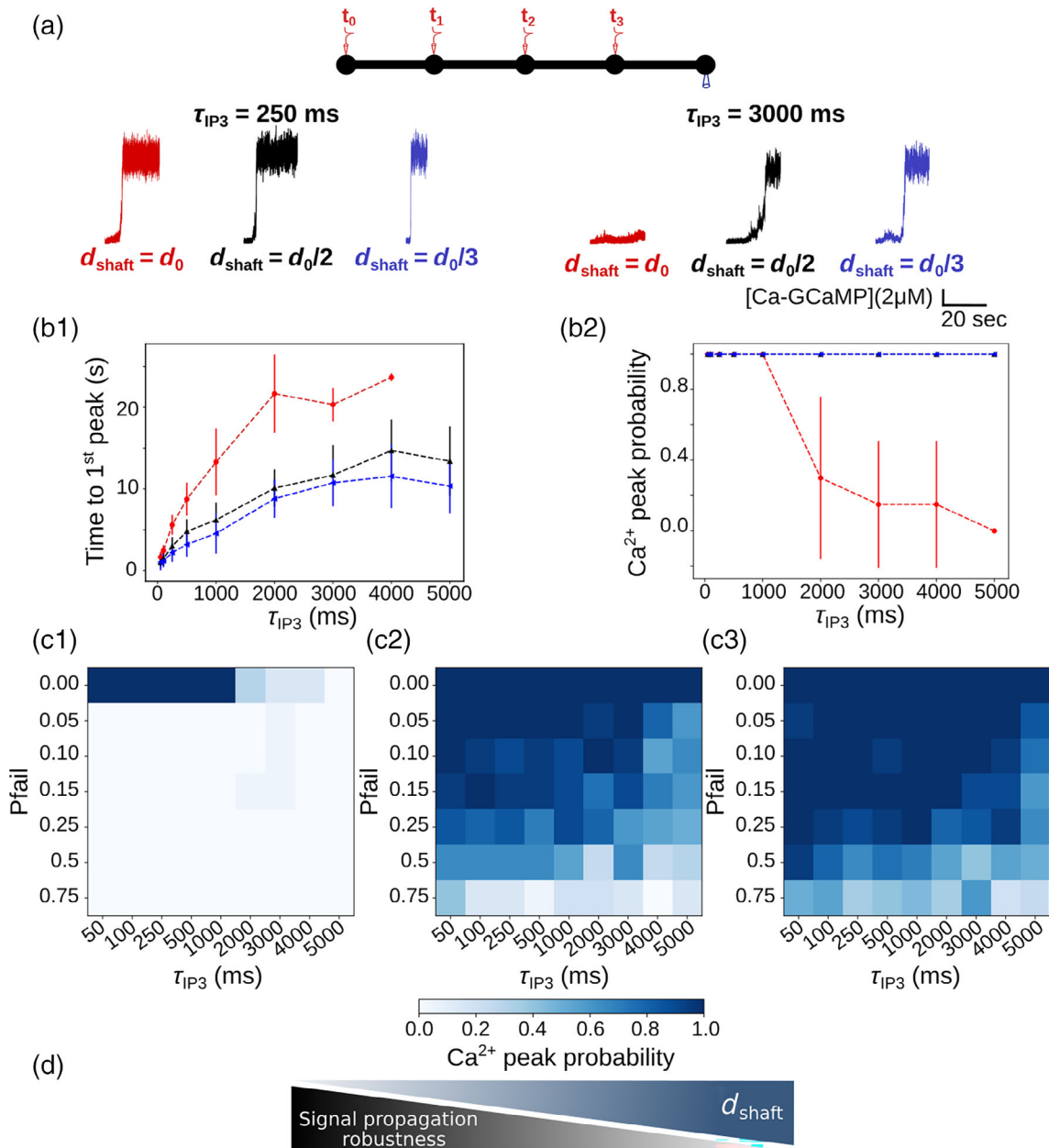


**FIGURE 5** Thin shafts favor a more robust signal propagation upon repeated neurotransmitter release events. (a) (top) Neuronal stimulation protocol: Node 1 is stimulated at  $t = t_0 = 5$  s, node 2 at  $t_0 + \tau_{\text{IP3}}$ , node 3 at  $t_0 + 2\tau_{\text{IP3}}$  and node 4 at  $t_0 + 3\tau_{\text{IP3}}$ ,  $k_{\text{Ca}} = 0 \text{ s}^{-1}$ .  $\text{Ca}^{2+}$  activity is recorded in node 5. (bottom) representative  $\text{Ca}^{2+}$  traces in node 5 for shaft width  $d_{\text{shaft}} = d_0$  (red),  $\frac{d_0}{2}$  (black) and  $\frac{d_0}{3}$  (blue), with  $\tau_{\text{IP3}} = 250$  ms (left) and  $3000$  ms (right), expressed as SNR (see Methods). For all values of  $\tau_{\text{IP3}}$  tested, simulation time was 25 s. (b1) Time to 1<sup>st</sup> peak increases with  $\tau_{\text{IP3}}$  for  $d_{\text{shaft}} = d_0$  (\*\*\*),  $\frac{d_0}{2}$  (\*\*\*) and  $\frac{d_0}{3}$  (\*\*\*). *T*-tests revealed that for any value of  $\tau_{\text{IP3}}$ , time to 1<sup>st</sup> peak is higher for  $d_{\text{shaft}} = d_0$  compared to  $d_{\text{shaft}} = \frac{d_0}{2}$  and  $\frac{d_0}{3}$ . Time to 1<sup>st</sup> peak is significantly higher when  $d_{\text{shaft}} = \frac{d_0}{2}$  compared to  $d_{\text{shaft}} = \frac{d_0}{3}$ , for most values of  $\tau_{\text{IP3}}$  ( $p = 0.032^*$ ,  $0.0025^{**}$ ,  $0.034^*$ ,  $0.016^*$ , and  $0.019^*$  for  $\tau_{\text{IP3}} = 250, 500, 1000, 4000$ , and  $5000$  ms, respectively). (b2)  $\text{Ca}^{2+}$  peak probability in node 5 is lower for  $d_{\text{shaft}} = d_0$  compared to  $d_{\text{shaft}} = \frac{d_0}{2}$  and  $\frac{d_0}{3}$ .  $\text{Ca}^{2+}$  peak probability decreases as  $\tau_{\text{IP3}}$  increases for  $d_{\text{shaft}} = d_0$  (\*\*\*). (c)  $\text{Ca}^{2+}$  peak probability in node 5 (colorbar) as a function of  $\tau_{\text{IP3}}$  and of the probability of failure of node stimulation  $p_{\text{fail}}$ , for  $d_{\text{shaft}} = d_0$  (c1),  $d_{\text{shaft}} = \frac{d_0}{2}$  (c2) and  $d_{\text{shaft}} = \frac{d_0}{3}$  (c3), with  $p_{\text{fail}} \in [0, 1]$ . (d) Schematic summarizing the main conclusion of this figure: Decreased shaft width allows signal propagation despite omitted node stimulation, thus favoring more robust signal propagation. Data are represented as mean  $\pm$  STD,  $n = 20$  for each value of  $d_{\text{shaft}}$  and of  $\tau_{\text{IP3}}$ . Lines in panel B are guides for the eyes.

1 is stimulated at  $t = t_0 = 5$  s, node 2 at  $t_0 + \tau_{IP3}$ , node 3 at  $t_0 + 2\tau_{IP3}$  and node 4 at  $t_0 + 3\tau_{IP3}$ . Neuronal stimulation is simulated as an infusion of 50 IP<sub>3</sub> molecules in the stimulated node. Representative Ca<sup>2+</sup> traces in node 5 in branchlets with various shaft widths  $d_{shaft}$  are presented in Figure 5a for  $\tau_{IP3} = 250$  and 3000 ms. Our first notable result is that the time to 1<sup>st</sup> peak in node 5 decreases with  $d_{shaft}$ , whatever the value of  $\tau_{IP3}$  (Figure 5b1). More specifically, time to 1<sup>st</sup> peak is higher for  $d_{shaft} = d_0$  compared to both  $d_{shaft} = \frac{d_0}{2}$  and  $\frac{d_0}{3}$ , while differences between  $d_{shaft} = \frac{d_0}{2}$  and  $\frac{d_0}{3}$  are not as striking. Moreover, the difference between  $d_{shaft} = d_0$ ,  $\frac{d_0}{2}$  and  $\frac{d_0}{3}$  increases with  $\tau_{IP3}$ . This suggests that geometries with  $d_{shaft} = d_0$  better discriminate slow from fast frequency of node stimulation compared to geometries with thinner shafts. Geometries with  $d_{shaft} = d_0$  are further characterized by a lower Ca<sup>2+</sup> peak probability in node 5 compared to geometries with  $d_{shaft} = \frac{d_0}{2}$  and  $\frac{d_0}{3}$  (Figure 5b2). More precisely, Ca<sup>2+</sup> peak probability decreases as  $\tau_{IP3}$  increases for  $d_{shaft} = d_0$ , which was observed independently of our boundary conditions (Figure S11, see Methods). Interestingly, the same effect was observed with various node stimulation patterns, where nodes were stimulated in a different order (Figure S12a) or where a single node was repeatedly stimulated (Figure S12b, c). This suggests that geometries with larger shafts could be associated with decreased signal propagation to remote nodes in case of repeated node stimulation at low frequency ( $\tau_{IP3} > 2$  s).

For  $\tau_{IP3} = 4$  s and  $d_{shaft} = \frac{d_0}{3}$ , signals were detected in node 5  $11.55 \pm 3.89$  s after the stimulation of node 1, which means that they occurred before the stimulation of node 4 ( $t = t_0 + 12$  s for  $\tau_{IP3} = 4$  s). This phenomenon was not observed for  $d_{shaft} = d_0$ , for which time to 1<sup>st</sup> peak when  $\tau_{IP3} = 4$  s was  $23.67 \pm 0.47$  s. This suggests that for  $d_{shaft} = \frac{d_0}{3}$ , contrary to  $d_{shaft} = d_0$ , one node stimulation could be omitted without having any consequence on Ca<sup>2+</sup> peak probability in node 5. In order to test this hypothesis, we have performed simulations in which the stimulation of nodes 2, 3 and 4 occurred with a given probability of failure  $p_{fail}$ . Simulations were performed for  $p_{fail} = 0, 0.05, 0.1, 0.15, 0.25$  and  $0.75$ . Ca<sup>2+</sup> peak probability in node 5, depending on  $p_{fail}$  and on  $\tau_{IP3}$  is presented in Figure 5c, for  $d_{shaft} = d_0$  (Figure 5c1),  $d_{shaft} = \frac{d_0}{2}$  (Figure 5c2) and  $d_{shaft} = \frac{d_0}{3}$  (Figure 5c3). As expected, Ca<sup>2+</sup> peak probability, despite high values of  $p_{fail}$ , increases when  $d_{shaft}$  decreases. Thus, thin shafts can favor signal propagation by allowing the omission of a node stimulation. In that sense, geometries displaying thin shafts are characterized by a more robust signal propagation (Figure 5d).

Together, our results suggest that, in the context of repeated node stimulation, thin shafts are associated with an increase of Ca<sup>2+</sup> peak probability in more remote nodes, with an earlier signal onset, suggesting increased signal propagation. Astrocytic processes with thicker shafts (here  $d_{shaft} = d_0$ ), such as observed in hypo-osmotic conditions (Arizono, Inavalli, et al. 2021), are associated with lower signal propagation in case of low stimulation frequency (time period  $> 2$  s), potentially favoring the formation of local Ca<sup>2+</sup> hotspots. Our results suggest that geometries with thick shafts could impair signal propagation when a branchlet is stimulated at a low frequency. In that sense, astrocyte branchlets with thicker shafts would be better detectors of the surrounding level of neuronal activity. By contrast,

branchlets with thin shafts would be less discriminating and provide more robust signal propagation.

## 4 | DISCUSSION

Fine astrocytic processes are responsible for most astrocytic Ca<sup>2+</sup> signals (Bindocci et al. 2017) and are preferential sites of neuron-astrocyte communication (Arizono et al. 2020). A better understanding of the mechanistic link between their morphology and the spatio-temporal properties of local Ca<sup>2+</sup> signals is crucial, yet hard to test experimentally. Here, we perform reaction-diffusion simulations in idealized morphologies of astrocytic processes derived from 3D super-resolution microscopy to investigate the effect of astrocyte nanoscale morphology on Ca<sup>2+</sup> activity in the gliapil. Our simulation results indicate that the nanoscale morphological features of astrocytic processes effectively increase the peak probability, duration, amplitude and propagation of Ca<sup>2+</sup> signals. Conversely, the alteration of the node-shaft arrangement of the spongiform domain associated with astrocyte swelling attenuates local Ca<sup>2+</sup> activity and signal propagation. Our simulation results, in accordance with experimental data, suggest that thin shafts effectively decrease diffusion flux, resulting in an increased compartmentalization of biochemical signals in nodes. Thus, nodes, similarly to dendritic spines (Santamaria et al. 2011), act as diffusion traps when shaft width is low. Note that, more than the value of shaft width itself, our results emphasize the effect of the ratio between node and shaft diameter on Ca<sup>2+</sup> activity. The simple geometries that we have evaluated in this study could be used to build a more comprehensive model of the spongiform structure to simulate Ca<sup>2+</sup> activity in the entire astrocyte. By recording the molecular interactions resulting in Ca<sup>2+</sup> signals upon neuronal stimulation in small cellular compartments of the gliapil, which cannot be performed experimentally, our simulation results shed light on the mechanisms by which the nano-architecture of astrocytic processes influences the frequency, amplitude and propagation of local Ca<sup>2+</sup> signals at tripartite synapses in health and disease.

Experimental Ca<sup>2+</sup> recordings of astrocyte activity have established that astrocyte processes display both highly localized microdomain signals and propagating Ca<sup>2+</sup> waves (Srinivasan et al. 2015; Bindocci et al. 2017). Our simulations suggest that the morphology of the cell and of its organelles can strongly influence the formation of these patterns of astrocytic Ca<sup>2+</sup> signaling. Notably, thinner shafts allow less discriminating and more robust signal propagation upon repeated stimuli compared to larger shafts. On the contrary, geometries with thick shafts seem to be more discriminating, potentially favoring the propagation of signals resulting from repeated stimuli from co-active synapses. Cellular morphology thus emerges as a key parameter that regulates the active propagation of Ca<sup>2+</sup> signals. The ultrastructure of the spongiform domain of astrocytes is very complex, characterized by abundant branching points, conferring a reticular morphology (Arizono et al. 2020). Those branching points are reportedly sometimes arranged into ring-like structures, although their occurrence and shape are still debated and could differ depending on



the brain region under study (Arizono et al. 2020; Panatier et al. 2014; Kiyoshi et al. 2020; Salmon et al. 2021; Arizono and Nägerl 2021). The effect of this reticular ultrastructure on the propagation of  $\text{Ca}^{2+}$  signals remains to be uncovered. Further characterization of the shape of fine astrocytic processes of the spongiform domain, their variability as well as their connectivity to the neighboring synapses are thus required. Pairing those observations with biophysically-detailed models such as the one presented in this study stands to deepen our understanding of the roles of astrocytic and neuronal morphology at tripartite synapses on neuron-astrocyte communication.

In neurons, both experimental (Yuste et al. 2000; Noguchi et al. 2005; Tonnesen et al. 2014) and modeling (Schmidt and Eilers 2009; Biess et al. 2007; Simon et al. 2014; Bell et al. 2019; Holcman and Schuss 2005, 2011; Santamaria et al. 2011; Cugno et al. 2019) studies have suggested that thin spine necks favor the compartmentalization of  $\text{Ca}^{2+}$  signals within the spine head. This compartmentalization of synapses allows neurons to discriminate various inputs and to process information locally (Wybo et al. 2019, Poirazi and Papatzi 2020), increasing the computational power of the neuronal circuits. According to our simulation results, nodes connected to thin shafts could favor the emergence of large signals at the site of neuron-astrocyte communication. Interestingly, we further propose that those amplified signals in nodes, instead of resulting in  $\text{Ca}^{2+}$  hotspots, favor active signal propagation. Fine astrocytic processes encounter morphological rearrangements that are activity-dependent, which notably influence synaptic maturation, efficacy and spine stability (Theodosis et al. 2008; Zhou et al. 2019; Henneberger et al. 2020). Our study sheds light on the influence of rearrangements of the reticular morphology of fine processes on signal computation by astrocytes. Further investigation manipulating astrocyte morphology in situ as well as in vivo is required to better characterize the variability of astrocyte ultrastructure and the associated integration of  $\text{Ca}^{2+}$  signals.

The morphology of the complex spongiform domain of astrocytes is highly dynamic, subject to activity-dependent as well as pathological remodeling. Our study, providing mechanisms by which an altered astrocyte morphology influences neuron-astrocyte communication at the nanoscale, gives new insights into the involvement of astrocytes in brain function in health and disease.

#### AUTHOR CONTRIBUTION

AD, HB and EDS designed the study. UVN, EDS and HB supervised the work. AD implemented the code, conducted the simulations, and analyzed the computational data. Calcium imaging and analysis was performed by MA. AD wrote the first draft of the manuscript, which was revised and approved by all authors.

#### ACKNOWLEDGMENTS

This work was funded by the Okinawa Institute of Science and Technology Graduate University and by JSPS (Japan Society for the Promotion of Science) Postdoctoral Fellowship for Research in Japan (Standard, P21733). We thank Iain Hepburn and Weiliang Chen of the Computational Neuroscience Unit, OIST, Japan for discussion on 3D meshes and STEPS.

#### CONFLICT OF INTEREST

The authors declare no competing financial interests.

#### DATA AVAILABILITY STATEMENT

The simulation code and meshes used in this study are available at <http://modeldb.yale.edu/266928>.

#### ORCID

Audrey Denizot <https://orcid.org/0000-0002-3336-0163>

Misa Arizono <https://orcid.org/0000-0002-7726-6531>

U. Valentin Nägerl <https://orcid.org/0000-0001-6831-9008>

Hugues Berry <https://orcid.org/0000-0003-3470-683X>

Erik De Schutter <https://orcid.org/0000-0001-8618-5138>

#### REFERENCES

- Agarwal, A., Wu, P.-H., Hughes, E. G., Fukaya, M., Tischfield, M. A., Langseth, A. J., Wirtz, D., & Bergles, D. E. (2017, February). Transient opening of the mitochondrial permeability transition pore induces microdomain calcium transients in astrocyte processes. *Neuron*, 93(3), 587–605.e7. <https://doi.org/10.1016/j.neuron.2016.12.034>
- Ahmadpour, N., Kantroo, M., & Stobart, J. L. (2021). Extracellular calcium influx pathways in astrocyte calcium microdomain physiology. *Biomolecules*, 11(10), 1467. <https://doi.org/10.3390/biom11101467>
- Arizono, M., Bancelin, S., Bethge, P., Chéreau, R., Idziak, A., Inavalli, V. V. G. K., Pfeiffer, T., Tønnesen, J., & Nägerl, U. V. (2021). Nanoscale imaging of the functional anatomy of the brain. *Neuroforum*, 27(2), 67–77. <https://doi.org/10.1515/nf-2021-0004>
- Arizono, M., Inavalli, V. V. G. K., Bancelin, S., Fernández-Monreal, M., & Nägerl, U. V. (2021). Super-resolution shadow imaging reveals local remodeling of astrocytic microstructures and brain extracellular space after osmotic challenge. *Glia*, 69(6), 1605–1613. <https://doi.org/10.1002/glia.23995>
- Arizono, M., Inavalli, V. V. G. K., Panatier, A., Pfeiffer, T., Angibaud, J., Levat, F., Ter Veer, M. J. T., Stobart, J., Bellocchio, L., Mikoshiba, K., Marsicano, G., Weber, B., Oliet, S. H. R., & Nägerl, U. V. (2020). Structural basis of astrocytic  $\text{Ca}^{2+}$  signals at tripartite synapses. *Nature Communications*, 11(1), 1–15. <https://doi.org/10.1038/s41467-020-15648-4>
- Arizono, M., & Nägerl, U. V. (2021). Deciphering the functional nano-anatomy of the tripartite synapse using stimulated emission depletion microscopy. *Glia*, 70, 607–618. <https://doi.org/10.1002/glia.24103>
- Bartol, T. M., Keller, D. X., Kinney, J. P., Bajaj, C. L., Harris, K. M., Sejnowski, T. J., & Kennedy, M. B. (2015). Computational reconstitution of spine calcium transients from individual proteins. *Frontiers in Synaptic Neuroscience*, 7, 17. <https://doi.org/10.3389/fnsyn.2015.00017>
- Bell, M., Bartol, T., Sejnowski, T., & Rangamani, P. (2019). Dendritic spine geometry and spine apparatus organization govern the spatiotemporal dynamics of calcium. *The Journal of General Physiology*, 151(8), 1017–1034. <https://doi.org/10.1085/jgp.201812261>
- Bezprozvanny, I., Watras, J., & Ehrlich, B. E. (1991). Bell-shaped calcium-response curves of  $\text{ins}(1,4,5)\text{P}_3$ - and calcium-gated channels from endoplasmic reticulum of cerebellum. *Nature*, 351(6329), 751–754. <https://doi.org/10.1038/351751a0>
- Biess, A., Korkotian, E., & Holcman, D. (2007). Diffusion in a dendritic spine: The role of geometry. *Physical Review E*, 76(2), 21922. <https://doi.org/10.1103/PhysRevE.76.021922>
- Bindocci, E., Savtchouk, I., Liaudet, N., Becker, D., Carriero, G., & Volterra, A. (2017). Three-dimensional  $\text{Ca}^{2+}$  imaging advances understanding of astrocyte biology. *Science*, 356(6339), eaai8185. <https://doi.org/10.1126/science.aai8185>

- Brazhe, A. R., Postnov, D. E., & Sosnovtseva, O. (2018). Astrocyte calcium signaling: Interplay between structural and dynamical patterns. *Chaos: An Interdisciplinary Journal of Nonlinear Science*, 28(10), 106320. <https://doi.org/10.1063/1.5037153>
- Bushong, E. A., Martone, M. E., Jones, Y. Z., & Ellisman, M. H. (2002). Protoplasmic astrocytes in CA1 stratum radiatum occupy separate anatomical domains. *The Journal of Neuroscience: The Official Journal of the Society for Neuroscience*, 22(1), 183–192.
- Cali, C., Agus, M., Kare, K., Boges, D. J., Lehtvaslaihio, H., Hadwiger, M., & Magistretti, P. J. (2019). 3D cellular reconstruction of cortical glia and parenchymal morphometric analysis from serial block-face electron microscopy of juvenile rat. *Progress in Neurobiology*, 183, 101696. <https://doi.org/10.1016/j.pneurobio.2019.101696>
- Cugno, A., Bartol, T. M., Sejnowski, T. J., Iyengar, R., & Rangamani, P. (2019, August). Geometric principles of second messenger dynamics in dendritic spines. *Scientific Reports*, 9(1), 1–18. <https://doi.org/10.1038/s41598-019-48028-0>
- De Young, G. W., & Keizer, J. (1992). A single-pool inositol 1,4,5-trisphosphate-receptorbased model for agonist-stimulated oscillations in  $\text{Ca}^{2+}$  concentration. *Proceedings of the National Academy of Sciences*, 89(20), 9895–9899. <https://doi.org/10.1073/pnas.89.20.9895>
- Denizot, A., Arizono, M., Nägerl, U. V., Soula, H., & Berry, H. (2019). Simulation of calcium signaling in fine astrocyte processes: Effect of spatial properties on spontaneous activity. *PLoS Computational Biology*, 15(8), e1006795. <https://doi.org/10.1371/journal.pcbi.1006795>
- Di Castro, M. A., Chuquet, J., Liaudet, N., Bhaukaurally, K., Santello, M., Bouvier, D., Tiret, P., & Volterra, A. (2011). Local  $\text{Ca}^{2+}$  detection and modulation of synaptic release by astrocytes. *Nature Neuroscience*, 14(10), 1276–1284. <https://doi.org/10.1038/nn.2929>
- Francis, M., Qian, X., Charbel, C., Ledoux, J., Parker, J. C., & Taylor, M. S. (2012). Automated region of interest analysis of dynamic  $\text{Ca}^{2+}$  signals in image sequences. *American Journal of Physiology-Cell Physiology*, 303(3), C236–C243. <https://doi.org/10.1152/ajpcell.00016.2012>
- Gähwiler, B. H. (1981). Organotypic monolayer cultures of nervous tissue. *Journal of Neuroscience Methods*, 4(4), 329–342. [https://doi.org/10.1016/0165-0270\(81\)90003-0](https://doi.org/10.1016/0165-0270(81)90003-0)
- Giaume, C., & Venance, L. (1998). Intercellular calcium signaling and gap junctional communication in astrocytes. *Glia*, 24(1), 50–64. [https://doi.org/10.1002/\(SICI\)1098-1136\(199809\)24:1<50::AID-GLIA6>3.0.CO;2-4](https://doi.org/10.1002/(SICI)1098-1136(199809)24:1<50::AID-GLIA6>3.0.CO;2-4)
- Gillespie, D. T. (1977). Exact stochastic simulation of coupled chemical reactions. *The Journal of Physical Chemistry*, 81(25), 2340–2361. <https://doi.org/10.1021/j100540a008>
- Grosche, J., Matyash, V., Möller, T., Verkhratsky, A., Reichenbach, A., & Kettenmann, H. (1999). Microdomains for neuron–glia interaction: Parallel fiber signaling to Bergmann glial cells. *Nature Neuroscience*, 2(2), 139–143. <https://doi.org/10.1038/5692>
- Haustein, M. D., Kracun, S., Lu, X.-H., Shih, T., Jackson-Weaver, O., Tong, X., Xu, J., Yang, X. W., O'Dell, T. J., Marvin, J. S., Ellisman, M. H., Bushong, E. A., Looger, L. L., & Khakh, B. S. (2014). Conditions and constraints for astrocyte calcium signaling in the hippocampal mossy fiber pathway. *Neuron*, 82(2), 413–429. <https://doi.org/10.1016/j.neuron.2014.02.041>
- Henneberger, C., Bard, L., Panatier, A., Reynolds, J. P., Kopach, O., Medvedev, N. I., Minge, D., Herde, M. K., Anders, S., Kraev, I., Heller, J. P., Rama, S., Zheng, K., Jensen, T. P., Sanchez-Romero, I., Jackson, C. J., Janovjak, H., Ottersen, O. P., Nagelhus, E. A., ... Rusakov, D. A. (2020). LTP induction boosts glutamate spillover by driving withdrawal of Perisynaptic Astroglia. *Neuron*, 108(5), 919–936. <https://doi.org/10.1016/j.neuron.2020.08.030>
- Hepburn, I., Chen, W., Wils, S., & De Schutter, E. (2012). STEPS: Efficient simulation of stochastic reaction–diffusion models in realistic morphologies. *BMC Systems Biology*, 6(1), 36. <https://doi.org/10.1186/1752-0509-6-36>
- Holcman, D., & Schuss, Z. (2005). Modeling calcium dynamics in dendritic spines. *SIAM Journal on Applied Mathematics*, 65(3), 1006–1026. <https://doi.org/10.1137/S003613990342894X>
- Holcman, D., & Schuss, Z. (2011). Diffusion laws in dendritic spines. *The Journal of Mathematical Neuroscience*, 1(1), 10. <https://doi.org/10.1186/2190-8567-1-10>
- Kiyoshi, C. M., Aten, S., Arzola, E. P., Patterson, J. A., Taylor, A. T., Du, Y., Guiher, A. M., Philip, M., Camacho, E. G., Mediratta, D., Collins, K., Benson, E., Kidd, G., Terman, D., & Zhou, M. (2020). Ultrastructural view of astrocyte-astrocyte and astrocyte-synapse contacts within the hippocampus. *bioRxiv*, 2020.10.28.358200. doi: <https://doi.org/10.1101/2020.10.28.358200>
- Lafrenaye, A. D., & Simard, J. M. (2019). Bursting at the seams: Molecular mechanisms mediating astrocyte swelling. *International Journal of Molecular Sciences*, 20(2), 330. <https://doi.org/10.3390/ijms20020330>
- Lee, H.-G., Wheeler, M. A., & Quintana, F. J. (2022). Function and therapeutic value of astrocytes in neurological diseases. *Nature Reviews Drug Discovery*, 21, 1–20. <https://doi.org/10.1038/s41573-022-00390-x>
- Lind, B. L., Brazhe, A. R., Jessen, S. B., Tan, F. C. C., & Lauritzen, M. J. (2013). Rapid stimulus-evoked astrocyte  $\text{Ca}^{2+}$  elevations and hemodynamic responses in mouse somatosensory cortex in vivo. *Proceedings of the National Academy of Sciences*, 110, E4687. <https://doi.org/10.1073/pnas.1310065110>
- Majewska, A., Brown, E., Ross, J., & Yuste, R. (2000). Mechanisms of calcium decay kinetics in hippocampal spines: Role of spine calcium pumps and calcium diffusion through the spine neck in biochemical compartmentalization. *Journal of Neuroscience*, 20(5), 1722–1734. <https://doi.org/10.1523/JNEUROSCI.20-05-01722.2000>
- McDougal, R. A., Morse, T. M., Carnevale, T., Marengo, L., Wang, R., Migliore, M., Miller, P. L., Shepherd, G. M., & Hines, M. L. (2017). Twenty years of ModelDB and beyond: Building essential modeling tools for the future of neuroscience. *Journal of Computational Neuroscience*, 42(1), 1–10. <https://doi.org/10.1007/s10827-016-0623-7>
- Nedergaard, M., Rodríguez, J. J., & Verkhratsky, A. (2010). Glial calcium and diseases of the nervous system. *Cell Calcium*, 47(2), 140–149. <https://doi.org/10.1016/j.ceca.2009.11.010>
- Noguchi, J., Matsuzaki, M., Ellis-Davies, G. C. R., & Kasai, H. (2005). Spine-neck geometry determines NMDA receptor-dependent  $\text{Ca}^{2+}$  signaling in dendrites. *Neuron*, 46(4), 609–622. <https://doi.org/10.1016/j.neuron.2005.03.015>
- Otsu, Y., Couchman, K., Lyons, D. G., Collot, M., Agarwal, A., Mallet, J.-M., Pfrieger, F. W., Bergles, D. E., & Charpak, S. (2015, February). Calcium dynamics in astrocyte processes during neurovascular coupling. *Nature Neuroscience*, 18(2), 210–218. <https://doi.org/10.1038/nn.3906>
- Panatier, A., Arizono, M., & Nägerl, U. V. (2014). Dissecting tripartite synapses with STED microscopy. *Philosophical Transactions of the Royal Society B*, 369 (1654), 20130597. doi: <https://doi.org/10.1098/rstb.2013.0597>
- Panatier, A., Vallée, J., Haber, M., Murai, K. K., Lacaille, J.-C., & Robitaille, R. (2011). Astrocytes are endogenous regulators of basal transmission at central synapses. *Cell*, 146(5), 785–798. <https://doi.org/10.1016/j.cell.2011.07.022>
- Poirazi, P., & Papoutsis, A. (2020). Illuminating dendritic function with computational models. *Nature Reviews Neuroscience*, 21(6), 303–321. <https://doi.org/10.1038/s41583-020-0301-7>
- Reichenbach, A., Derouiche, A., & Kirchhoff, F. (2010). Morphology and dynamics of perisynaptic glia. *Brain Research Reviews*, 63(1–2), 11–25. <https://doi.org/10.1016/j.brainresrev.2010.02.003>
- Rusakov, D. A. (2015). Disentangling calcium-driven astrocyte physiology. *Nature Reviews Neuroscience*, 16(4), 226–233. <https://doi.org/10.1038/nrn3878>

- Salmon, C. K., Syed, T. A., Kacerovsky, J. B., Alivodej, N., Schober, A. L., Pratte, M. T., Rosen, M. P., Green, M., DasGupta, A., Vali, H., Mandato, C. A., Siddiqi, K., & Murai, K. K. (2021). Organizing principles of astrocytic nanoarchitecture in the mouse cerebral cortex (Tech. Rep.). doi: <https://doi.org/10.1101/2021.11.05.467391>
- Santamaria, F., Wils, S., De Schutter, E., & Augustine, G. J. (2011). The diffusional properties of dendrites depend on the density of dendritic spines. *The European Journal of Neuroscience*, 34(4), 561–568. <https://doi.org/10.1111/j.1460-9568.2011.07785.x>
- Schmidt, H., & Eilers, J. (2009). Spine neck geometry determines spino-dendritic crosstalk in the presence of mobile endogenous calcium binding proteins. *Journal of Computational Neuroscience*, 27(2), 229–243. <https://doi.org/10.1007/s10827-009-0139-5>
- Schuss, Z., Singer, A., & Holcman, D. (2007). The narrow escape problem for diffusion in cellular microdomains. *Proceedings of the National Academy of Sciences*, 104(41), 16098–16103. <https://doi.org/10.1073/pnas.0706599104>
- Semyanov, A., Henneberger, C., & Agarwal, A. (2020). Making sense of astrocytic calcium signals – From acquisition to interpretation. *Nature Reviews Neuroscience*, 21(10), 1–14. <https://doi.org/10.1038/s41583-020-0361-8>
- Sherwood, M. W., Arizono, M., Hisatsune, C., Bannai, H., Ebisui, E., Sherwood, J. L., Panatier, A., Oliet, S. H. R., & Mikoshiba, K. (2017). Astrocytic IP3Rs: Contribution to Ca<sup>2+</sup> signalling and hippocampal LTP. *Glia*, 65(3), 502–513. <https://doi.org/10.1002/glia.23107>
- Shigetomi, E., Bushong, E. A., Haustein, M. D., Tong, X., Jackson-Weaver, O., Kracun, S., Xu, J., Sofroniew, M. V., Ellisman, M. H., & Khakh, B. S. (2013). Imaging calcium microdomains within entire astrocyte territories and endfeet with GCaMPs expressed using adeno-associated viruses. *The Journal of General Physiology*, 141(5), 633–647. <https://doi.org/10.1085/jgp.201210949>
- Shigetomi, E., Patel, S., & Khakh, B. S. (2016). Probing the complexities of astrocyte calcium signaling. *Trends in Cell Biology*, 26(4), 300–312. <https://doi.org/10.1016/j.tcb.2016.01.003>
- Shigetomi, E., Saito, K., Sano, F., & Koizumi, S. (2019). Aberrant calcium signals in reactive astrocytes: A key process in neurological disorders. *International Journal of Molecular Sciences*, 20(4), 996. <https://doi.org/10.3390/ijms20040996>
- Simon, C. M., Hepburn, I., Chen, W., & Schutter, E. D. (2014). The role of dendritic spine morphology in the compartmentalization and delivery of surface receptors. *Journal of Computational Neuroscience*, 36(3), 483–497. <https://doi.org/10.1007/s10827-013-0482-4>
- Spacek, J., & Harris, K. M. (1997). Three-dimensional Organization of Smooth Endoplasmic Reticulum in hippocampal CA1 dendrites and dendritic spines of the immature and mature rat. *Journal of Neuroscience*, 17(1), 190–203. <https://doi.org/10.1523/JNEUROSCI.17-01-00190.1997>
- Srinivasan, R., Huang, B. S., Venugopal, S., Johnston, A. D., Chai, H., Zeng, H., Golshani, P., & Khakh, B. S. (2015). Ca<sup>2+</sup> signaling in astrocytes from *Ip3r2(-/-)* mice in brain slices and during startle responses in vivo. *Nature Neuroscience*, 18(5), 708–717. <https://doi.org/10.1038/nn.4001>
- Stobart, J. L., Ferrari, K. D., Barrett, M. J. P., Glück, C., Stobart, M. J., Zuend, M., & Weber, B. (2018). Cortical circuit activity evokes rapid astrocyte calcium signals on a similar timescale to neurons. *Neuron*, 98(4), 726–735.e4. <https://doi.org/10.1016/j.neuron.2018.03.050>
- Stobart, J. L., Ferrari, K. D., Barrett, M. J. P., Stobart, M. J., Looser, Z. J., Saab, A. S., & Weber, B. (2018). Long-term in vivo calcium imaging of astrocytes reveals distinct cellular compartment responses to sensory stimulation. *Cerebral Cortex (New York, N.Y.: 1991)*, 28(1), 184–198. <https://doi.org/10.1093/cercor/bhw366>
- Theodosis, D. T., Poulain, D. A., & Oliet, S. H. R. (2008). Activity-dependent structural and functional plasticity of astrocyte-neuron interactions. *Physiological Reviews*, 88(3), 983–1008. <https://doi.org/10.1152/physrev.00036.2007>
- Tonnesen, J., Katona, G., Rózsa, B., & Nägerl, U. V. (2014). Spine neck plasticity regulates compartmentalization of synapses. *Nature Neuroscience*, 17(5), 678–685. <https://doi.org/10.1038/nn.3682>
- Tonnesen, J., Nadrigny, F., Willig, K. I., Wedlich-Söldner, R., & Nägerl, U. V. (2011). Two-color STED microscopy of living synapses using a single laser-beam pair. *Biophysical Journal*, 101(10), 2545–2552. <https://doi.org/10.1016/j.bpj.2011.10.011>
- Urban, N. T., Willig, K. I., Hell, S. W., & Nägerl, U. V. (2011). STED Nano-scopy of Actin dynamics in synapses deep inside living brain slices. *Biophysical Journal*, 101(5), 1277–1284. <https://doi.org/10.1016/j.bpj.2011.07.027>
- Verkhatsky, A., & Nedergaard, M. (2018). Physiology of astroglia. *Physiological Reviews*, 98(1), 239–389. <https://doi.org/10.1152/physrev.00042.2016>
- Witcher, M. R., Kirov, S. A., & Harris, K. M. (2007). Plasticity of perisynaptic astroglia during synaptogenesis in the mature rat hippocampus. *Glia*, 55(1), 13–23. <https://doi.org/10.1002/glia.20415>
- Wu, Y.-W., Gordleeva, S., Tang, X., Shih, P.-Y., Dembitskaya, Y., & Semyanov, A. (2018). Morphological profile determines the frequency of spontaneous calcium events in astrocytic processes. bioRxiv, 410076. doi: <https://doi.org/10.1101/410076>
- Wybo, W. A. M., Torben-Nielsen, B., Nevian, T., & Gewaltig, M.-O. (2019). Electrical compartmentalization in neurons. *Cell Reports*, 26(7), 1759–1773.e7. <https://doi.org/10.1016/j.celrep.2019.01.074>
- Yasuda, R. (2017). Biophysics of biochemical signaling in dendritic spines: Implications in synaptic plasticity. *Biophysical Journal*, 113(10), 2152–2159. <https://doi.org/10.1016/j.bpj.2017.07.029>
- Yuste, R., Majewska, A., & Holthoff, K. (2000). From form to function: Calcium compartmentalization in dendritic spines. *Nature Neuroscience*, 3(7), 653–659. <https://doi.org/10.1038/76609>
- Zhou, B., Zuo, Y.-X., & Jiang, R.-T. (2019). Astrocyte morphology: Diversity, plasticity, and role in neurological diseases. *CNS neuroscience & therapeutics*, 25(6), 665–673. <https://doi.org/10.1111/cns.13123>

## SUPPORTING INFORMATION

Additional supporting information can be found online in the Supporting Information section at the end of this article.

**How to cite this article:** Denizot, A., Arizono, M., Nägerl, U. V., Berry, H., & De Schutter, E. (2022). Control of Ca<sup>2+</sup> signals by astrocyte nanoscale morphology at tripartite synapses. *Glia*, 1–14. <https://doi.org/10.1002/glia.24258>

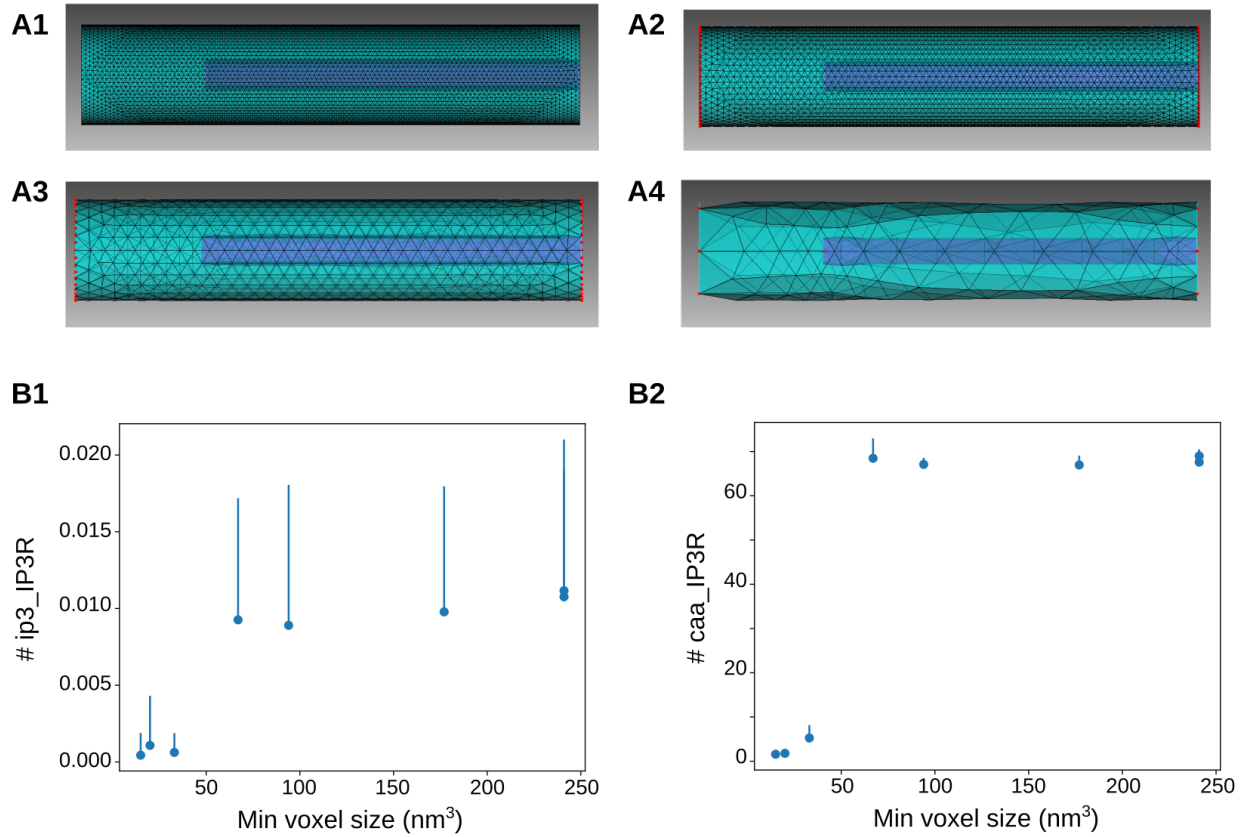


**Figure S1. Sensitivity study of the effect of voxel size on  $\text{Ca}^{2+}$  signals.** (A) Simulations were performed in a cylinder geometry with various numbers of tetrahedra. 4 examples are presented here, “*Cyl*<sub>1</sub>” (A1), “*Cyl*<sub>3</sub>” (A2), “*Cyl*<sub>5</sub>” (A3) and “*Cyl*<sub>8</sub>” (A4). Please refer to Table ?? for details on the characteristics of each mesh. (B) Study of the average number of IP<sub>3</sub>R in the ip3\_IP3R state (IP<sub>3</sub> bound to its binding site on IP<sub>3</sub>R, B1) and in the caa\_IP3R state ( $\text{Ca}^{2+}$  bound to the activating site of IP<sub>3</sub>R, B2) depending on the minimum voxel size of the mesh.



Geom	# tet	$V_{\text{mean}}$	$V_{\text{std}}$	$V_{\text{max}}$	$V_{\text{min}}$	Diff ( $nm^3$ )	Diff (%)
<i>Cyl</i> <sub>1</sub>	372148	84	25	296	15	281	335
<i>Cyl</i> <sub>2</sub>	274233	115	34	389	20	369	321
<i>Cyl</i> <sub>3</sub>	125927	249	71	761	33	728	292
<i>Cyl</i> <sub>4</sub>	40077	782	229	2200	67	2133	273
<i>Cyl</i> <sub>5</sub>	11523	2700	790	7521	177	7344	272
<i>Cyl</i> <sub>6</sub>	3103	9900	3200	24000	94	23906	241
<i>Cyl</i> <sub>7</sub>	1417	21000	11000	62000	241	61759	294
<i>Cyl</i> <sub>8</sub>	945	32000	28000	145000	241	144759	452

**Table S1. Characteristics of meshes used to investigate the effect of voxel size on  $Ca^{2+}$  signals.** Cylinder geometries were generated with various total number of tetrahedra (geometry *Cyl*<sub>*i*</sub> with *i* ∈ [1, 8], see also Fig S1A), resulting in different voxel sizes.  $V_{\text{mean}}$  corresponds to the average voxel volume,  $V_{\text{std}}$  to its standard deviation,  $V_{\text{max}}$  to the maximum voxel volume and  $V_{\text{min}}$  to the minimum voxel volume in the mesh. Volumes are expressed in  $nm^3$ . Diff ( $nm^3$ ) corresponds to  $V_{\text{max}} - V_{\text{min}}$  while Diff (%) is the ratio  $\frac{V_{\text{max}} - V_{\text{min}}}{V_{\text{mean}}} * 100$

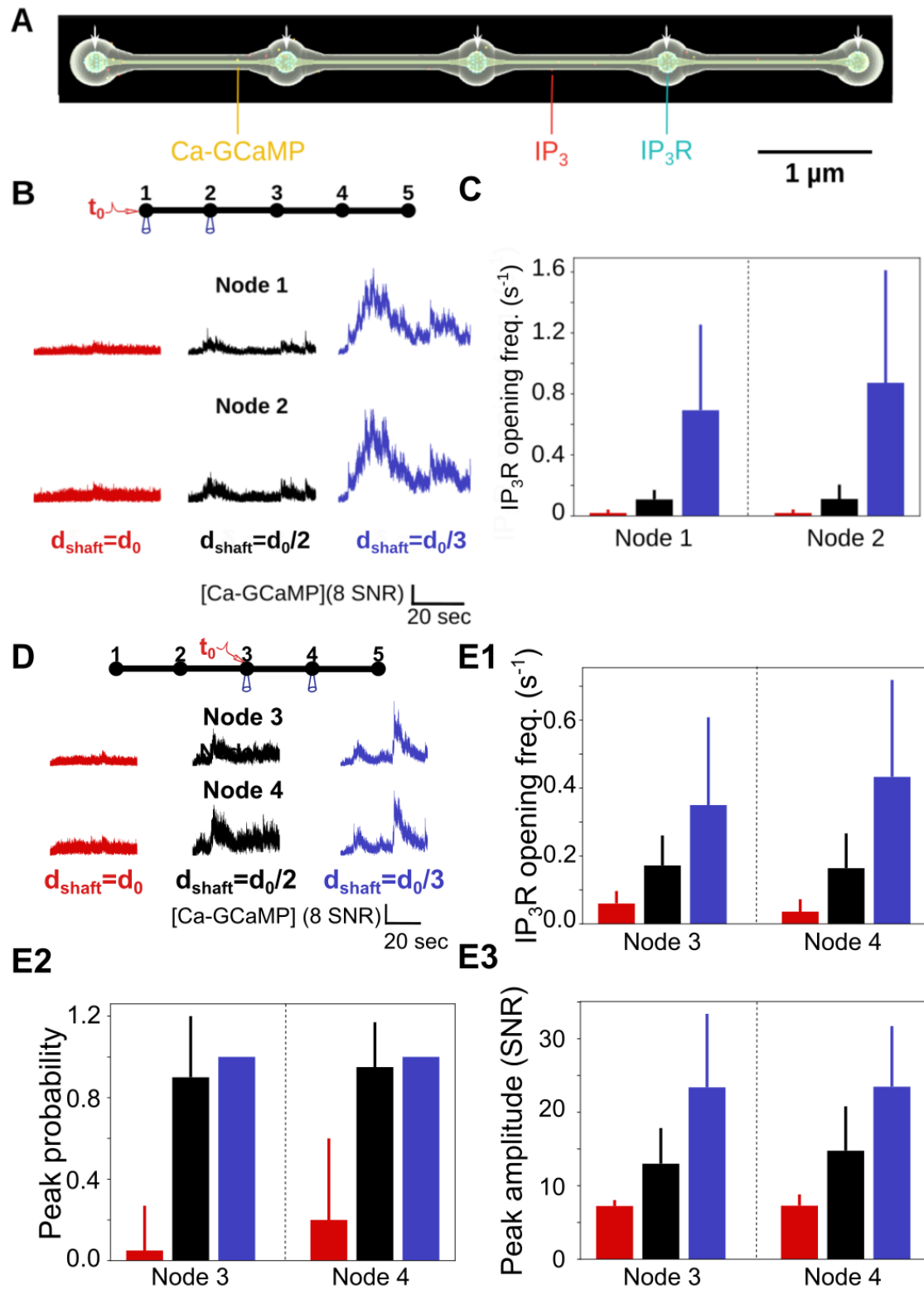
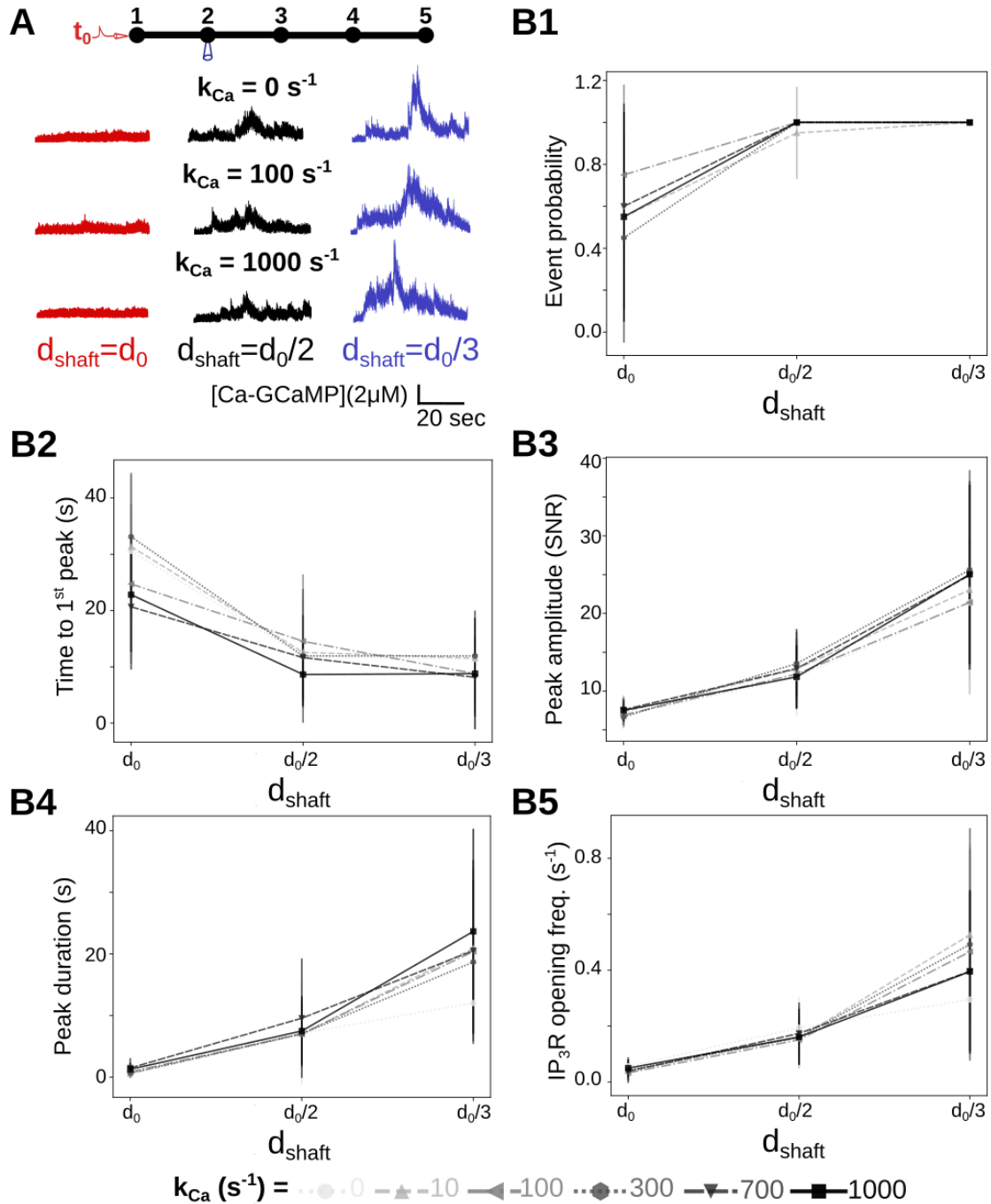


Figure S2. Sensitivity study of the effect of shaft width on local  $\text{Ca}^{2+}$  signals upon

**single node stimulation.** (A) Screenshot of a simulation in the “5nodes”  $d_{\text{shaft}} = \frac{d_0}{3}$  geometry. In those simulations, IP<sub>3</sub>R channels are only positioned on the ER membrane in nodes (white arrows). The number of IP<sub>3</sub>R channels is 300 for all values of  $d_{\text{shaft}}$ . (B) (Top) Node 1 was stimulated at  $t=t_0=1\text{s}$ , while  $\text{Ca}^{2+}$  activity was monitored in nodes 1 and 2. (Bottom) Representative  $\text{Ca}^{2+}$  traces in node 1 and node 2 for  $d_{\text{shaft}}=d_0$  (red),  $\frac{d_0}{2}$  (black) and  $\frac{d_0}{3}$  (blue). (C) The frequency of IP<sub>3</sub>R opening increases with  $d_{\text{shaft}}$  decreases in nodes 1 (\*\*\*) and 2 (\*\*\*). (D) (Top) In a second set of simulations, node 3 was stimulated at  $t=t_0=1\text{s}$  ( $k_{Ca}=0\text{ s}^{-1}$ ), while  $\text{Ca}^{2+}$  activity was monitored in nodes 3 and 4. (Bottom) Representative [Ca-GCaMP] traces in nodes 3 and 4, expressed as SNR (see Methods), for  $d_{\text{shaft}}=d_0$  (red),  $\frac{d_0}{2}$  (black) and  $\frac{d_0}{3}$  (blue). (E1) The frequency of IP<sub>3</sub>R opening increases when  $d_{\text{shaft}}$  decreases in node 3 (\*\*\*) and 4 (\*\*\*). (E2)  $\text{Ca}^{2+}$  peak probability increases when  $d_{\text{shaft}}$  decreases in node 3 (\*\*\*) and 4 (\*\*\*). (E3) Peak amplitude increases when  $d_{\text{shaft}}$  decreases in node 3 (\*\*\*) and 4 (\*\*\*). Data are represented as mean  $\pm$  STD,  $n=20$  for each geometry. The effect of  $d_{\text{shaft}}$  on each  $\text{Ca}^{2+}$  signal characteristic was tested using one-way ANOVA. Significance is assigned by \* for  $p \leq 0.05$ , \*\* for  $p \leq 0.01$ , \*\*\* for  $p \leq 0.001$ .



**Figure S3. Effect of  $\text{Ca}^{2+}$  influx rate at the plasma membrane on local  $\text{Ca}^{2+}$  signals.** A) (Top) Neuronal stimulation protocol simulated for each geometry: node 1 was stimulated at  $t=t_0=1\text{s}$ , while  $\text{Ca}^{2+}$  activity was monitored in node 2. Representative  $\text{Ca}^{2+}$  traces for shaft width  $d_{\text{shaft}} = d_0$  (red),  $\frac{d_0}{2}$  (black) and  $\frac{d_0}{3}$  (blue), with a  $\text{Ca}^{2+}$  influx rate at the plasma membrane  $k_{Ca}=0$  (top), 100 (middle) and  $1000 \text{ s}^{-1}$  (bottom), expressed as SNR (see Methods). (B) Quantification of the effect of  $d_{\text{shaft}}$  on  $\text{Ca}^{2+}$  signal characteristics for  $k_{Ca}=0, 10, 100, 300, 700$  and  $1000 \text{ s}^{-1}$ . Data are

represented as mean  $\pm$  STD, n=20 for each set of parameters tested.  $\text{Ca}^{2+}$  peak probability increases (\*\*\*, *B1*), Time to 1<sup>st</sup> peak decreases (\*\*\*, *B2*), peak amplitude (\*\*\*, *B3*) and duration (\*\*\*, *B4*) increase when  $d_{\text{shaft}}$  decreases, for  $k_{\text{Ca}}=0, 10, 100, 300, 700$  and  $1000 \text{ s}^{-1}$ .  $\text{Ca}^{2+}$  peak characteristics did not statistically vary with  $k_{\text{Ca}}$ . The effect of  $k_{\text{Ca}}$  on each  $\text{Ca}^{2+}$  signal characteristic was tested using one-way ANOVA.

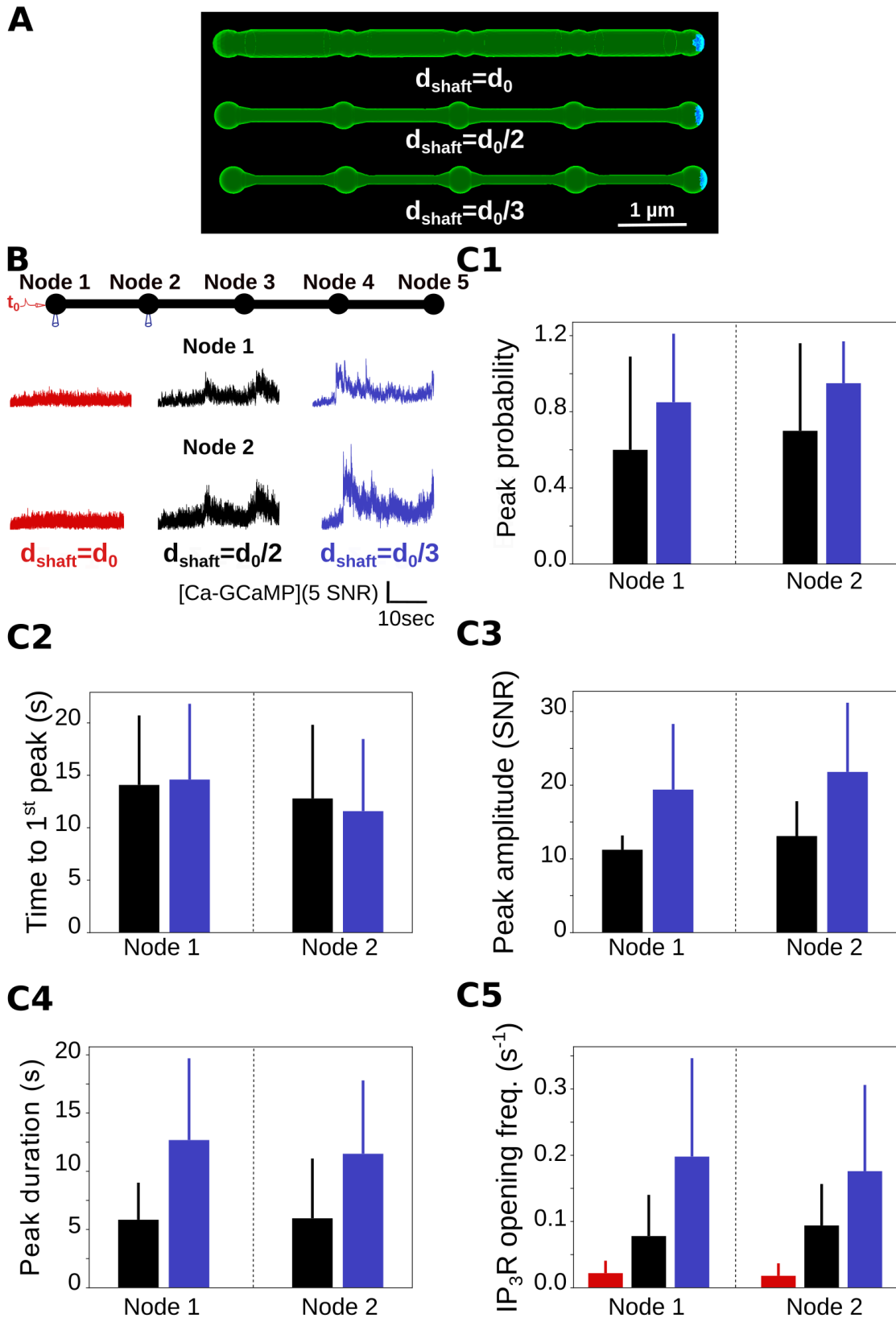


**Figure S4. Sensitivity study of the effect of boundary conditions on local  $\text{Ca}^{2+}$  activity upon single node stimulation.** (A) Geometries used in the simulations were the “5nodes” geometries (Fig1B). Boundary conditions were absorbing at the extremity of node 5 (blue), while the remaining boundaries were reflective (green). This mimics the connection of the modeled astrocyte branchlet to the rest of the cell. (B) (Top) Neuronal stimulation protocol simulated for each geometry: node 1 was stimulated at  $t=t_0=1\text{s}$  ( $k_{Ca}=0\text{ s}^{-1}$ ), while  $\text{Ca}^{2+}$  activity was monitored in nodes 1 and 2. (Bottom) Representative [Ca-GCaMP] traces in nodes 1 and 2, expressed as SNR (see Methods), for  $d_{\text{shaft}}=d_0$  (red),  $\frac{d_0}{2}$  (black) and  $\frac{d_0}{3}$  (blue). (C1)  $\text{Ca}^{2+}$  peak probability increases when  $d_{\text{shaft}}$  decreases in nodes 1 (\*\*\*) and 2 (\*\*\*). (C2) Time to 1<sup>st</sup> peak does not change with  $d_{\text{shaft}}$ , both in node 1 (p-value=0.85) and 2 (p-value=0.90). (C3) Peak amplitude increases when  $d_{\text{shaft}}$  decreases in nodes 1 (p-value=0.0056 \*\*) and 2 (p-value=0.0021 \*\*). (C4) Peak duration increases when  $d_{\text{shaft}}$  decreases in nodes 1 (p-value=0.0051 \*\*) and 2 (p-value=0.014 \*). (C5) The frequency of  $\text{IP}_3\text{R}$  opening increases when  $d_{\text{shaft}}$  decreases in both nodes 1 and 2 (\*\*\*). Note that there were no  $\text{Ca}^{2+}$  peak in simulations with  $d_{\text{shaft}}=d_0$ .  $\text{Ca}^{2+}$  peak characteristics were not statistically different between node 1 and 2. Data are represented as mean  $\pm$  STD,  $n=20$  for each geometry. The effect of  $d_{\text{shaft}}$  on each  $\text{Ca}^{2+}$  signal characteristic was tested using one-way ANOVA. Significance is assigned by \* for  $p \leq 0.05$ , \*\* for  $p \leq 0.01$ , \*\*\* for  $p \leq 0.001$ .

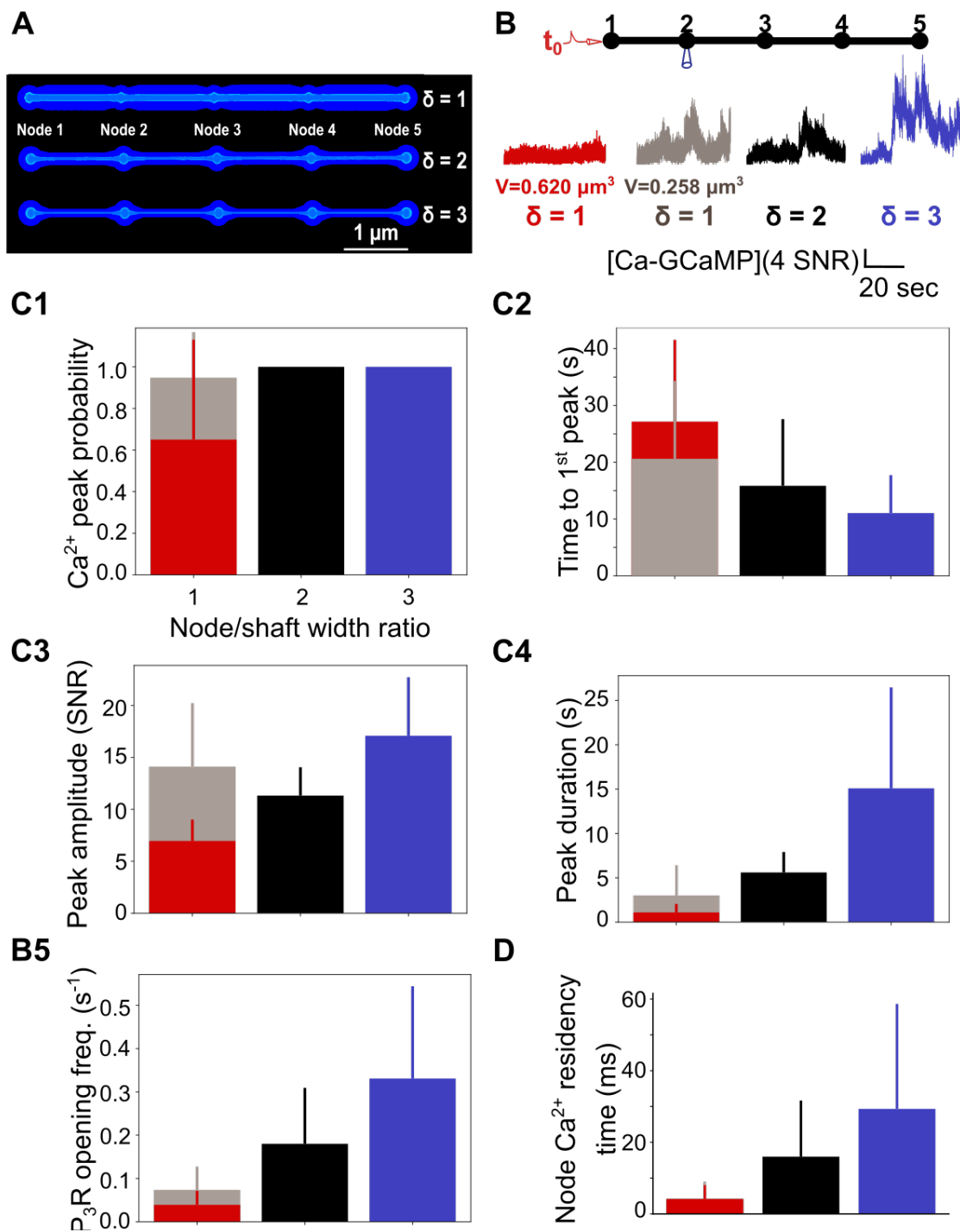


**Figure S5. Node/shaft width ratio and node volume control local Ca<sup>2+</sup> activity.** (A) Screenshots from STEPS visualization toolkit revealing meshes used in this study, that contain 5 identical nodes and 4 identical shafts. (B) (Top) Neuronal stimulation protocol simulated for each geometry: node 1 was stimulated at  $t=t_0=1\text{s}$  ( $k_{Ca}=0 \text{ s}^{-1}$ ), while Ca<sup>2+</sup> activity was recorded in node 2. (Bottom) Representative Ca<sup>2+</sup> traces in node 2 in geometries with node/shaft width ratio



$\delta = \frac{d_0}{d_{\text{shaft}}} = 1$  (red and gray), 2 (black) and 3 (blue), expressed as SNR (see Methods). Red and grey traces correspond to  $\text{Ca}^{2+}$  signals in geometries with  $\delta=1$  and a volume  $V_1=0.620 \mu\text{m}^3$  and  $V_1=0.258 \mu\text{m}^3$ , respectively. Black and blue traces were recorded in geometries with  $V_2=0.263 \mu\text{m}^3$  and  $V_3=0.195 \mu\text{m}^3$ , respectively. (C) Quantification of  $\text{Ca}^{2+}$  signal characteristics depending on node/shaft width ratio  $\delta$  and on process volume. Data are represented as mean  $\pm$  STD, n=20 for each geometry. (C1)  $\text{Ca}^{2+}$  peak probability does not vary with  $\delta$  when  $V_1=0.258 \mu\text{m}^3$  (p-value=0.22). (C2) Time to 1<sup>st</sup> peak decreases with  $\delta$  (p-value=0.0018 \*). (C3) Peak amplitude does not vary with  $\delta$  when  $V_1=0.258 \mu\text{m}^3$  (p-value=0.16). (C4) Peak duration increases with  $\delta$ , for both  $V_1=0.620 \mu\text{m}^3$  and  $V_1=0.258 \mu\text{m}^3$  (\*\*\*). (C5) The frequency of  $\text{IP}_3\text{R}$  opening increases with  $\delta$ , for both  $V_1=0.620 \mu\text{m}^3$  and  $V_1=0.258 \mu\text{m}^3$  (\*\*\*). (D)  $\text{Ca}^{2+}$  residency time in nodes increases with  $\delta$ , for both  $V_1=0.620 \mu\text{m}^3$  and  $V_1=0.258 \mu\text{m}^3$  (\*\*\*, n=300). The effect of node/shaft width ratio on each  $\text{Ca}^{2+}$  signal characteristic was tested using one-way ANOVA. Significance is assigned by \* for  $p \leq 0.05$ , \*\* for  $p \leq 0.01$ , \*\*\* for  $p \leq 0.001$ .

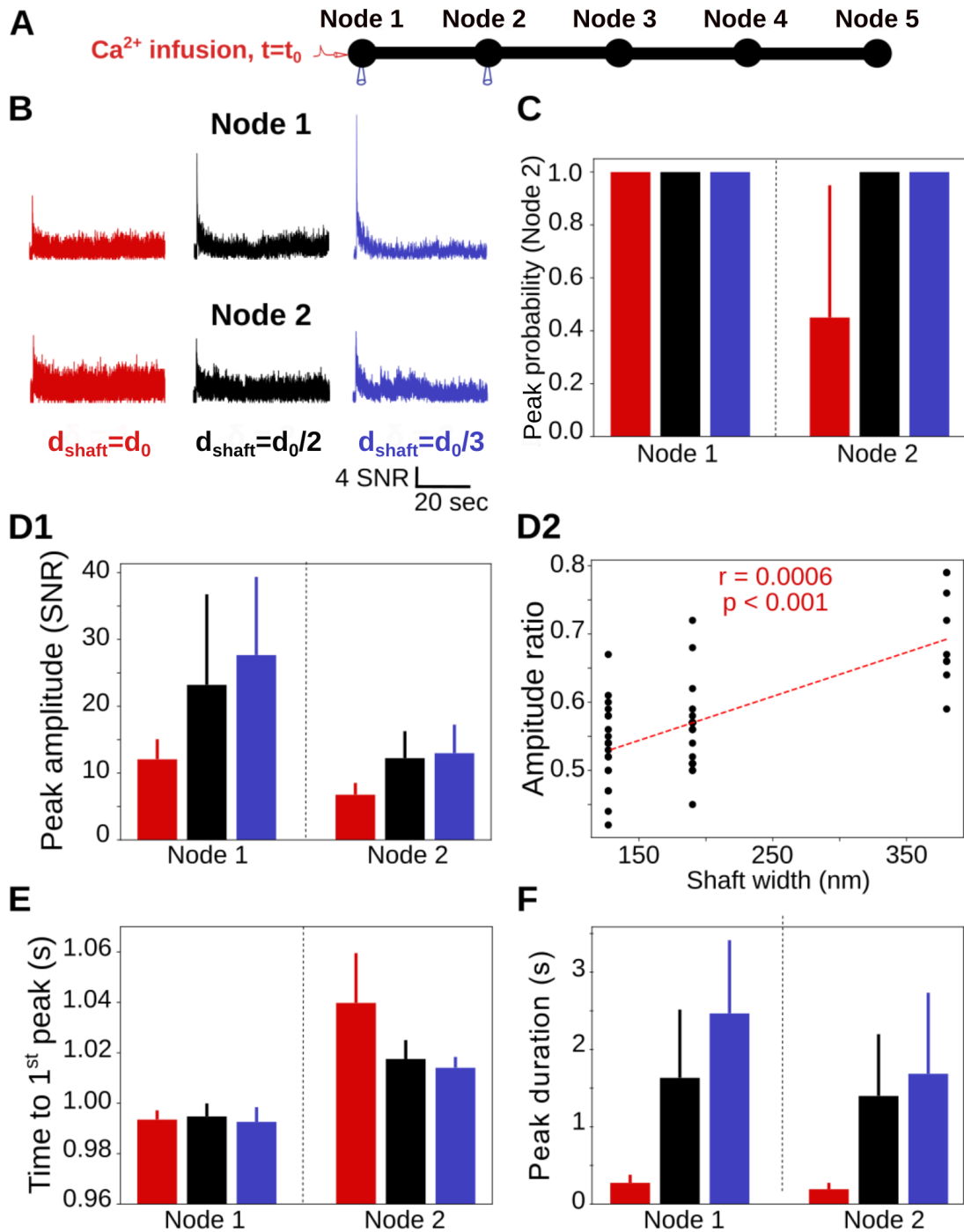


**Figure S6. Thin shafts enhance local spontaneous  $\text{Ca}^{2+}$  activity.** (A) Neuronal stimulation protocol simulated for each geometry. 200  $\text{Ca}^{2+}$  ions were infused in Node 1 at time  $t=t_0$ , while  $\text{Ca}^{2+}$  activity was recorded in nodes 1 and 2. (B) Representative  $\text{Ca}^{2+}$  traces in node 1 (top) and node 2 (bottom) for  $d_{\text{shaft}}=d_0$  (red),  $\frac{d_0}{2}$  (black) and  $\frac{d_0}{3}$  (blue), expressed as SNR (see Methods). (C)  $\text{Ca}^{2+}$  peak probability increases when  $d_{\text{shaft}}$  decreases in node 2 (\*\*\*) . Note that peak probability

is 1 in node 1 as the injection of 200  $\text{Ca}^{2+}$  ions in node 1 results in a local Ca-GCaMP peak for all seed values tested. (*D1*) Peak amplitude increases when  $d_{\text{shaft}}$  decreases in node 1 (\*\*\*) and 2 (\*\*\*). (*D2*) The ratio between peak amplitude in node 2 and in Node 1 increases with shaft width (Spearman  $r=0.0006$ ,  $p\text{-value} < 0.001$  \*\*\*). (*E*) Time to 1<sup>st</sup> peak in node 2 increases with  $d_{\text{shaft}}$  (\*\*\*). Note that time to 1<sup>st</sup> peak does not vary with  $d_{\text{shaft}}$  in node 1 as it occurs quickly after  $\text{Ca}^{2+}$  injection, through the binding of the injected  $\text{Ca}^{2+}$  ions to GCaMP molecules. (*F*) Peak duration increases when  $d_{\text{shaft}}$  decreases in node 1 (\*\*\*) and 2 (\*\*\*). Note that  $\text{Ca}^{2+}$  peak characteristics were not statistically different between nodes 1 and 2. Data are represented as mean  $\pm$  STD,  $n=20$  for each geometry. The effect of  $d_{\text{shaft}}$  on each  $\text{Ca}^{2+}$  signal characteristic was tested using one-way ANOVA. Significance is assigned by \* for  $p \leq 0.05$ , \*\* for  $p \leq 0.01$ , \*\*\* for  $p \leq 0.001$ .

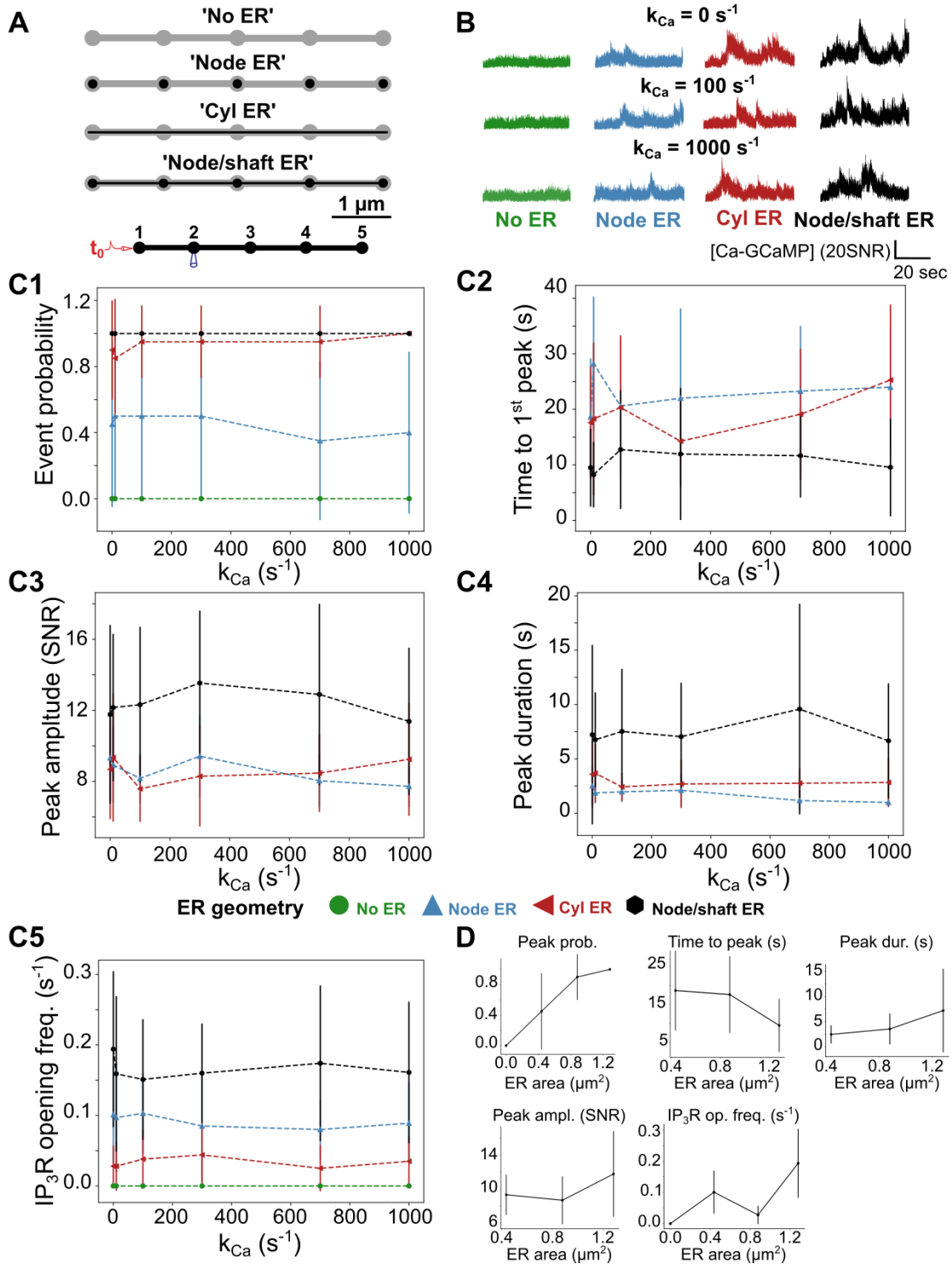


**Figure S7.**  $\text{Ca}^{2+}$  peak probability, amplitude and duration decrease with ER surface area. (A) As the shape and distribution of the ER in fine processes have not been characterized in live tissue so far but are likely highly variable, simulations were performed in meshes with various

ER shapes: “No ER”, “Node ER”, “Cyl ER” and “Node/shaft ER”, in which there was no ER, discontinuous ER in nodes, cylindrical ER, or an ER consisting in node/shaft alternations, respectively. (B) (*Top*) Neuronal stimulation protocol simulated for each geometry: node 1 was stimulated at  $t=t_0=1s$ , while  $Ca^{2+}$  activity was monitored in nodes 1 and 2. (*Bottom*) Representative  $Ca^{2+}$  traces in node 2, in “No ER” (green), “Node ER” (blue), “Cyl ER” (red) and “Node/shaft ER” (black) geometries  $d_{shaft}=\frac{d_0}{2}$ , for  $k_{Ca}=0, 10, 100, 300, 700$  and  $1000 s^{-1}$ , expressed as SNR (see Methods). (C) Quantification of peak characteristics depending on ER geometry and  $k_{Ca}$ .  $Ca^{2+}$  peak probability (\*\*\*, C1), time to 1<sup>st</sup> peak (\*\*\*, C2), peak amplitude (\*\*\*, C3), duration (\*\*\*, C4) and the frequency of IP<sub>3</sub>R opening (\*\*\*, C5) vary with ER morphology. Note that  $Ca^{2+}$  peak characteristics did not vary with  $k_{Ca}$ . (D) Time to 1<sup>st</sup> decreases as ER surface area increases (\*\*\*) while  $Ca^{2+}$  peak probability (\*\*\*), amplitude (\*\*\*) and duration (\*\*\*) as well as the frequency of IP<sub>3</sub>R opening (\*\*\*) increase as ER surface area increases,  $k_{Ca}=0 s^{-1}$ . Data are represented as mean  $\pm$  STD, n=20 for each geometry. Significance is assigned by \* for  $p \leq 0.05$ , \*\* for  $p \leq 0.01$ , \*\*\* for  $p \leq 0.001$ .

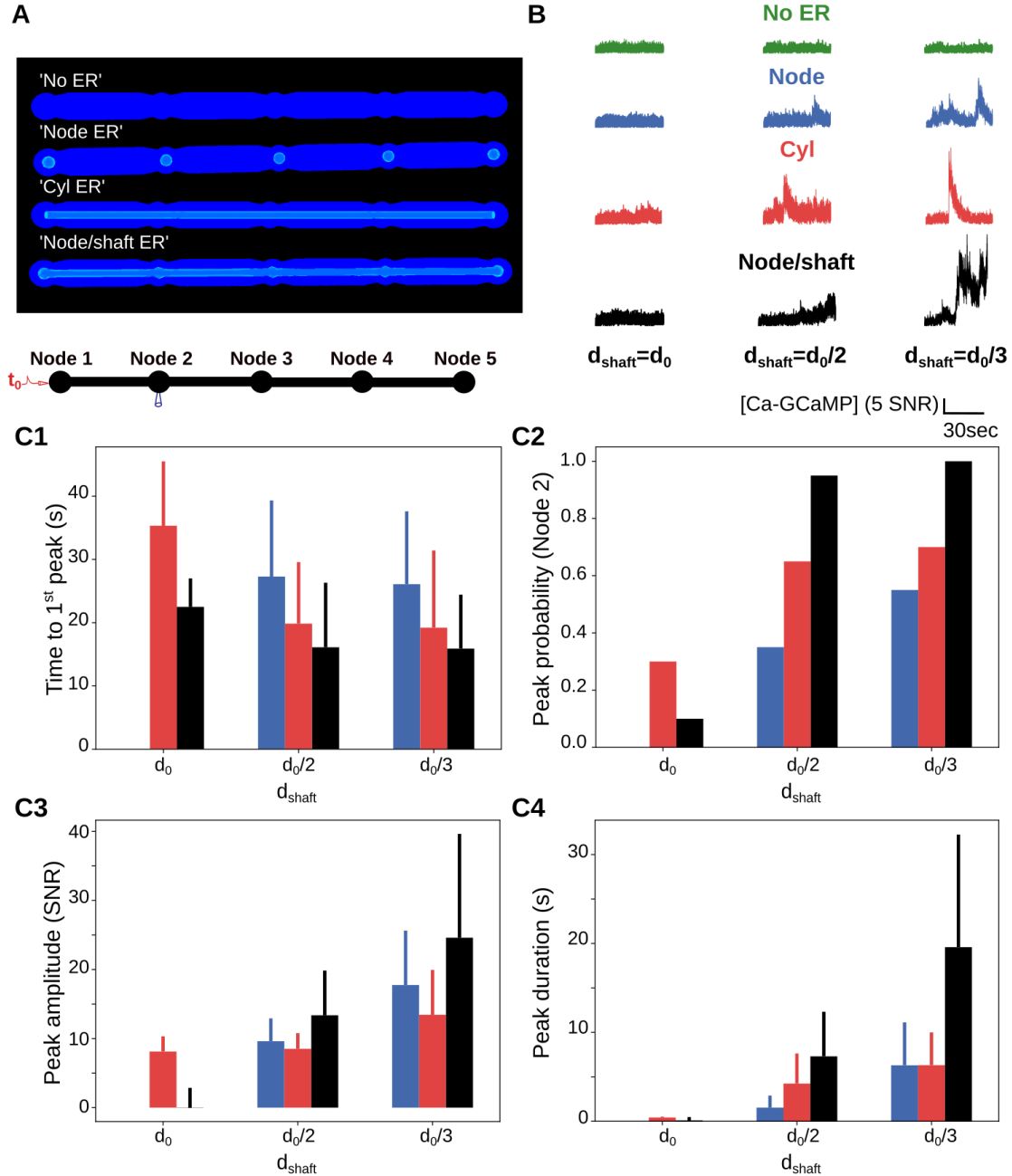


**Figure S8. Local  $\text{Ca}^{2+}$  activity increases when shaft diameter decreases, for all ER geometries tested.** (A) Screenshots displaying the 3D meshes used to investigate the effect of ER geometry on  $\text{Ca}^{2+}$  dynamics: “No ER”, “Node ER”, “Cyl ER” and “Node/shaft ER”. (B) (Top) Neuronal stimulation protocol simulated for each geometry: node 1 was stimulated at  $t=t_0=1\text{s}$  ( $k_{\text{Ca}}=0\text{ s}^{-1}$ ), while  $\text{Ca}^{2+}$  activity was monitored in node 2. (Bottom) Representative  $\text{Ca}^{2+}$  traces in node 2 for  $d_{\text{shaft}}=d_0$  (left),  $\frac{d_0}{2}$  (center) and  $\frac{d_0}{3}$  (right), in “No ER” (green), “Node ER” (blue),

“Cyl ER” (red) and “Node/shaft ER” (black) geometries, expressed as SNR (see Methods). (C) Quantification of the effect of  $d_{\text{shaft}}$  on  $\text{Ca}^{2+}$  dynamics. Note that no bar is visible for simulations in “Node ER”  $d_{\text{shaft}}=d_0$  geometries as no peak was detected. Results in “Node/shaft ER” geometries are presented in Fig3 but are added here (black bars) for comparison. (C1) Time to 1<sup>st</sup> peak in node 2 does not vary with  $d_{\text{shaft}}$  in “Node ER” simulations (p-value=0.85) but increases with  $d_{\text{shaft}}$  in “Cyl ER” simulations (p-value= 0.021 \*). (C2)  $\text{Ca}^{2+}$  peak probability in node 2 increases when  $d_{\text{shaft}}$  decreases in “Node ER” simulations (\*\*\*) and in “Cyl ER” simulations (p-value=0.01 \*). (C3) Peak amplitude increases when  $d_{\text{shaft}}$  decreases in “Node ER” geometries (p-value=0.027 \*) and in “Cyl ER” (p-value=0.01 \*). (C4) Peak duration increases when  $d_{\text{shaft}}$  decreases in “Node ER” simulations (p-value=0.028 \*) and in “Cyl ER” simulations (p-value=0.001 \*\*). Data are represented as mean  $\pm$  STD, n=20, for each geometry. The effect of  $d_{\text{shaft}}$  on each  $\text{Ca}^{2+}$  signal characteristic was tested using one-way ANOVA. Significance is assigned by \* for  $p \leq 0.05$ , \*\* for  $p \leq 0.01$ , \*\*\* for  $p \leq 0.001$ .

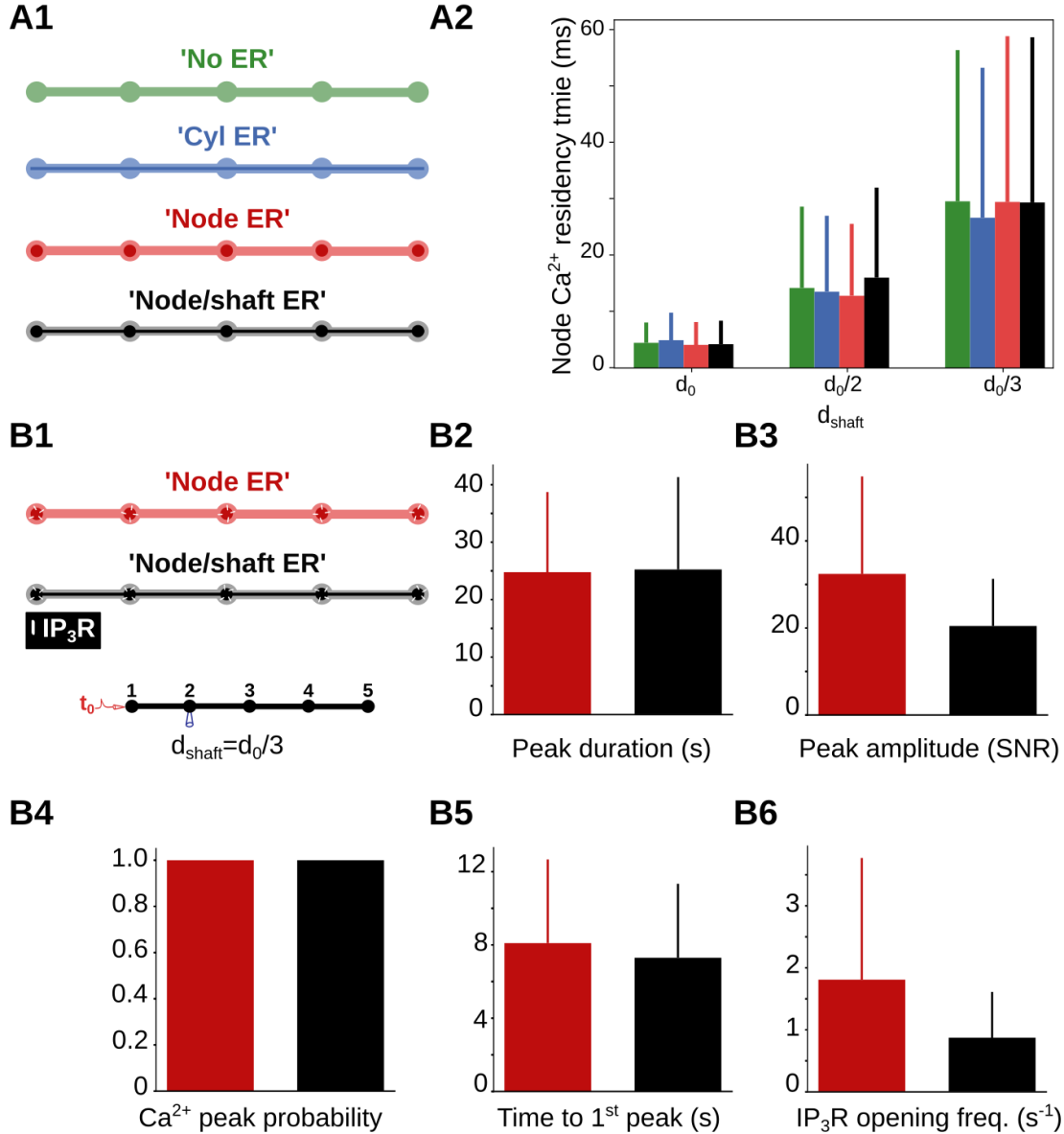


**Figure S9. Sensitivity study of the effect of ER morphology on Ca<sup>2+</sup> dynamics.** (A) Node Ca<sup>2+</sup> residency time is not influenced by ER morphology. (A1) One Ca<sup>2+</sup> ion was added in node 1 in geometries with different ER shapes: “No ER” (green), “Cyl ER” (blue), “Node ER” (red) and “Node/shaft ER” (black). (A2) For all ER shapes tested, Ca<sup>2+</sup> residency time in nodes increases when d<sub>shaft</sub> decreases. Node Ca<sup>2+</sup> residency time does not change depending on ER morphology, suggesting that cellular morphology has a greater influence on compartmentalization than ER morphology in the meshes used in this study. Data are represented as mean  $\leq$  STD, n=300 for each geometry. (B) Sensitivity study of the effect of ER morphology on Ca<sup>2+</sup> dynamics with constant number of IP<sub>3</sub>Rs. (B1) Simulations were performed in ‘Node ER’ (red) and “Node/shaft ER” (black) geometries with IP<sub>3</sub>R channels (white) located in nodes (Top), resulting in a constant number of IP<sub>3</sub>R channels for both ER shapes. Node 1 was stimulated at t=t<sub>0</sub>=1s ( $k_{Ca}=0$  s<sup>-1</sup>), while



$\text{Ca}^{2+}$  activity was monitored in node 2 (bottom). (B2-6) Quantification of  $\text{Ca}^{2+}$  signals depending on ER morphology with constant number of  $\text{IP}_3\text{R}$  in node 2,  $d_{\text{shaft}} = \frac{d_0}{3}$ . Data are represented as mean  $\pm$  STD,  $n=20$  for each geometry.  $\text{Ca}^{2+}$  peak duration (B2), amplitude (B3), probability (B4) and delay (B5) do not vary with ER morphology when  $\text{IP}_3\text{R}$  channels are located in nodes. (B6)  $\text{IP}_3\text{R}$  opening frequency does not significantly differ between “Node ER” and “Node/shaft ER” geometries (p-value=0.06). Those results suggest that the decreased  $\text{Ca}^{2+}$  activity in branchlets that contain discontinuous ER reported in Fig 4 mainly results from the decreased number of  $\text{IP}_3\text{R}$  channels associated with the decreased ER surface area of “Node ER” compared to “Node/shaft ER” morphology.

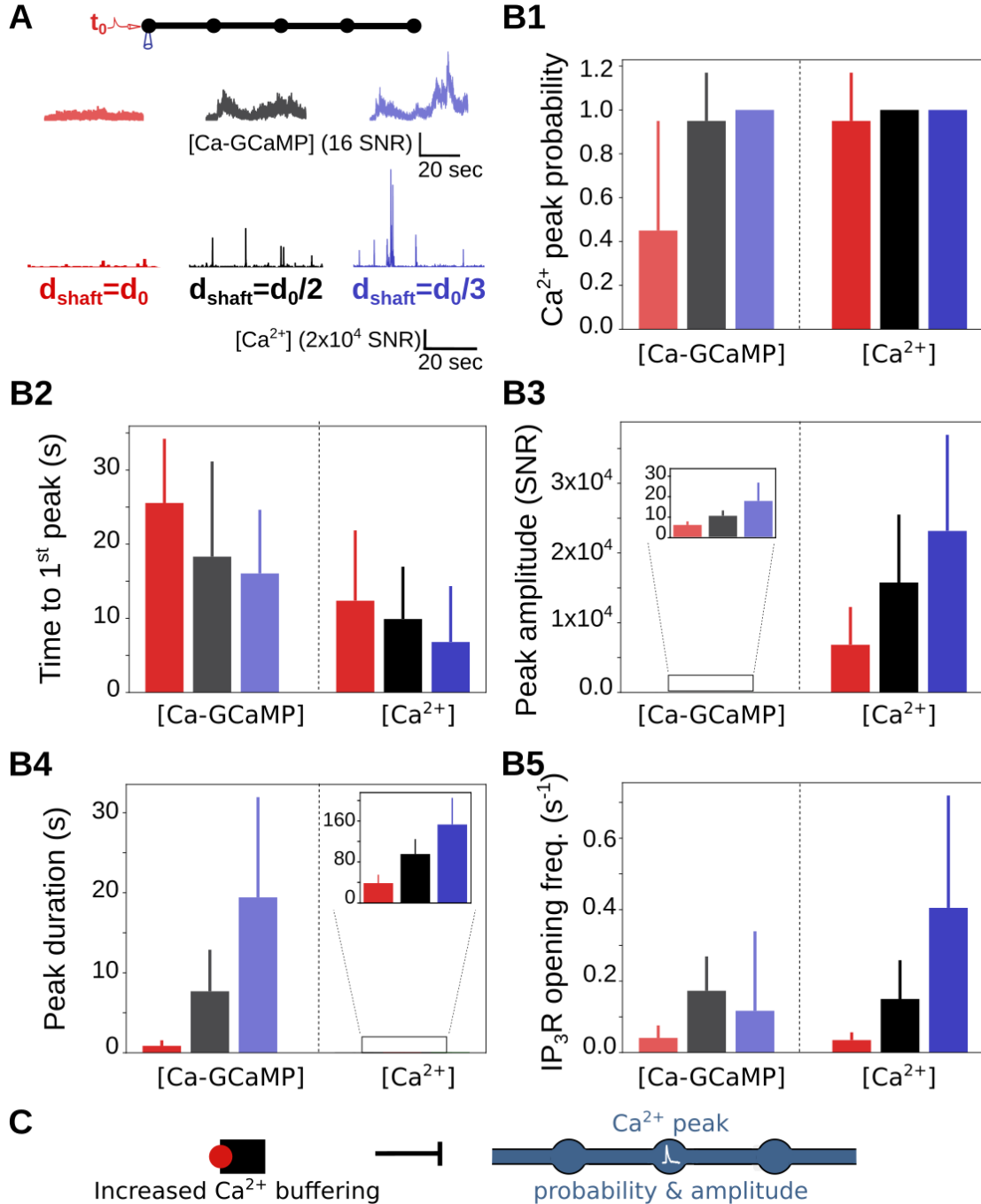


**Figure S10. Ca<sup>2+</sup> indicators alter Ca<sup>2+</sup> peak characteristics.** (A) In order to investigate free Ca<sup>2+</sup> peak probability, no GCaMP molecules were added to the model. (Top) At  $t=t_0=1$ s, node 1 was stimulated ( $k_{Ca}=0$  s<sup>-1</sup>), while Ca<sup>2+</sup> concentration was monitored in node 1. The geometry used for  $d_{\text{shaft}} = d_0$  corresponds to the geometry presented in Fig 1B. (Middle) Representative Ca-GCaMP traces in node 1, in simulations containing GCaMP molecules in geometries with shaft width  $d_{\text{shaft}} = d_0$  (light red),  $\frac{d_0}{2}$  (grey) and  $\frac{d_0}{3}$  (light blue). (Bottom) Representative free Ca<sup>2+</sup>

traces in node 1, in the absence of GCaMP molecules, in geometries with shaft width  $d_{\text{shaft}} = d_0$  (red),  $\frac{d_0}{2}$  (black) and  $\frac{d_0}{3}$  (blue). The amplitude of Ca-GCaMP and free  $\text{Ca}^{2+}$  signals is expressed as SNR (see Methods). (B) Characteristics of free  $\text{Ca}^{2+}$  signals depending on  $d_{\text{shaft}}$ . Ca-GCaMP signals measured in simulations from Fig 3 are presented for comparison. (B1) Free  $\text{Ca}^{2+}$  peak probability does not vary with  $d_{\text{shaft}}$  (p-value=0.22). Ca-GCaMP peak probability is lower than free  $\text{Ca}^{2+}$  peak probability for  $d_{\text{shaft}}=d_0$  (\*\*\*). (B2) Time to 1<sup>st</sup> free  $\text{Ca}^{2+}$  peak increases with  $d_{\text{shaft}}$  (\*\*\*). Time to 1<sup>st</sup> Ca-GCaMP peak is higher than time to 1<sup>st</sup> free  $\text{Ca}^{2+}$  peak, for any value of  $d_{\text{shaft}}$  (\*\*\*). (B3) Free  $\text{Ca}^{2+}$  peak amplitude increases when  $d_{\text{shaft}}$  decreases (\*\*\*). Ca-GCaMP peak amplitude is lower than free  $\text{Ca}^{2+}$  peak amplitude, for any value of  $d_{\text{shaft}}$  (\*\*\*). (B4) Free  $\text{Ca}^{2+}$  peak duration increases when  $d_{\text{shaft}}$  decreases (\*\*\*). Ca-GCaMP peak duration is higher than free  $\text{Ca}^{2+}$  peak duration, for any value of  $d_{\text{shaft}}$  (\*\*\*). (B5) The frequency of IP<sub>3</sub>R opening increases when  $d_{\text{shaft}}$  decreases (\*\*\*). (C) Schematic summarizing the main result from this figure: increased  $\text{Ca}^{2+}$  buffering is associated with decreased  $\text{Ca}^{2+}$  peak probability and amplitude. Data are represented as mean  $\pm$  STD, n=20 for each geometry. The effect of  $d_{\text{shaft}}$  on each free  $\text{Ca}^{2+}$  signal characteristic was tested using one-way ANOVA. Significance is assigned by \* for  $p \leq 0.05$ , \*\* for  $p \leq 0.01$ , \*\*\* for  $p \leq 0.001$ .

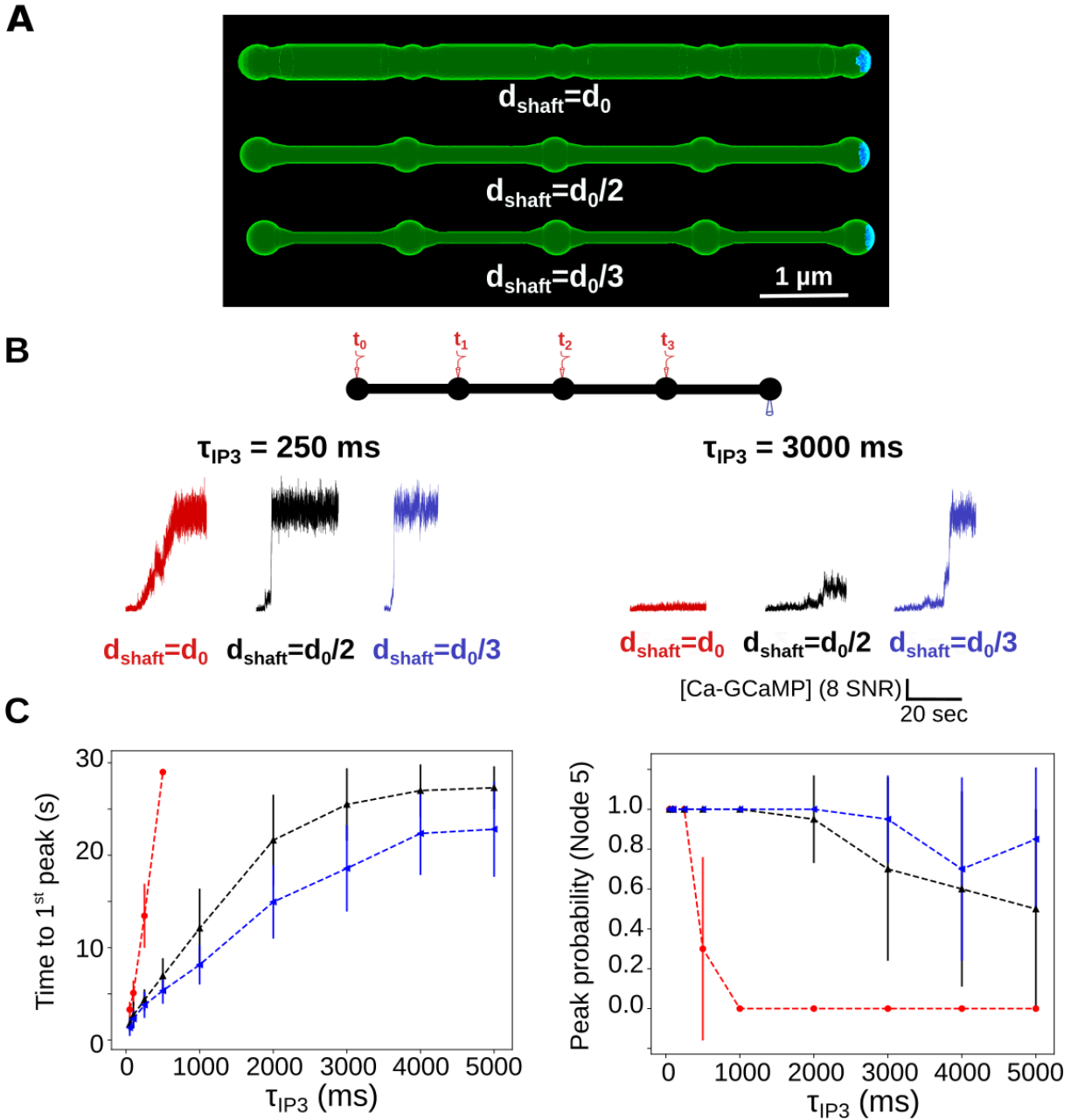


**Figure S11. Sensitivity study of the effect of boundary conditions on local  $\text{Ca}^{2+}$  activity upon repeated neuronal stimuli.** (A) Simulations were performed in the “5nodes” geometries (Fig1). Boundary conditions were absorbing at the extremity of node 5 (blue) while the remaining boundaries were characterized by reflective boundary conditions (green). Those boundary conditions mimic the connection of the modeled astrocyte branchlet to the rest of the cell. (B) (Top) node 1 was stimulated at  $t=t_0=5\text{s}$ , node 2 at  $t_0 + \tau_{\text{IP}_3}$ , node 3 at  $t_0 + 2\tau_{\text{IP}_3}$  and node 4 at  $t_0 + 3\tau_{\text{IP}_3}$ ,  $k_{\text{Ca}}=0 \text{ s}^{-1}$ , while  $\text{Ca}^{2+}$  activity was monitored in node 5. (Bottom) Representative  $\text{Ca}^{2+}$  traces for

$d_{\text{shaft}}=d_0$  (red),  $\frac{d_0}{2}$  (black) and  $\frac{d_0}{3}$  (blue), with  $\tau_{\text{IP3}}=250$  ms (left) and 3000 ms (right), expressed as SNR (see Methods). (C) (Left) Time to 1<sup>st</sup> peak in node 5 increases with  $\tau_{\text{IP3}}$  for  $d_{\text{shaft}}=d_0$  (\*\*\*) ,  $d_{\text{shaft}}=\frac{d_0}{2}$  (\*\*\*) and  $d_{\text{shaft}}=\frac{d_0}{3}$  (\*\*\*) . Time to 1<sup>st</sup> peak is higher for  $d_{\text{shaft}}=d_0$  compared to  $d_{\text{shaft}}=\frac{d_0}{2}$  and  $d_{\text{shaft}}=\frac{d_0}{3}$ . (Right)  $\text{Ca}^{2+}$  peak probability in node 5 is lower for  $d_{\text{shaft}}=d_0$  compared to  $d_{\text{shaft}}=\frac{d_0}{2}$  and  $d_{\text{shaft}}=\frac{d_0}{3}$  and decreases as  $\tau_{\text{IP3}}$  increases for  $d_{\text{shaft}}=d_0$  (\*\*\*) and  $d_{\text{shaft}}=\frac{d_0}{2}$  (\*\*\*) but not  $d_{\text{shaft}}=\frac{d_0}{3}$  (p-value=0.054). Note that  $\text{Ca}^{2+}$  peak probability was lower and time to 1<sup>st</sup> peak higher compared to simulations with reflective boundary conditions. Data are represented as mean  $\pm$  STD, n=20 for each value of  $d_{\text{shaft}}$  and of  $\tau_{\text{IP3}}$ . Lines are guides for the eyes. The effect of  $d_{\text{shaft}}$  on each  $\text{Ca}^{2+}$  signal characteristic was tested using one-way ANOVA. Significance is assigned by \* for  $p \leq 0.05$ , \*\* for  $p \leq 0.01$ , \*\*\* for  $p \leq 0.001$ .

## Movie S1

Movie presenting a simulation of the bleaching protocol, with  $d_{\text{shaft}} = \frac{d_0}{2}$ . Fluorescing ZsGreen molecules are in red and bleached, non-fluorescing, ZsGreen are in yellow. Molecule position was updated every 1 ms. The plot presents the variation of the number of fluorescing ZsGreen molecules with time in the central node. Note that, to facilitate visualization, here  $[\text{ZsGreen}] = 5 \mu\text{M}$ . Before the bleaching event, all ZsGreen proteins (red) fluoresce. At bleaching time, fluorescing molecules in the bleached region encounter conformational modifications that prevent them from fluorescing (yellow molecules). Consequently, the fluorescence level drops to  $I_0$ . Because of the diffusion of molecules in the cell, the fluorescence level in the central node then increases until it reaches a new baseline  $I_{\text{inf}}$ , after a recovery time  $\tau$ . Fluorescing ZsGreen molecules are in red and bleached, non-fluorescing, ZsGreen are in yellow.

## Movie S2

Movie presenting a simulation of the neuronal stimulation protocol, with  $d_{\text{shaft}} = \frac{d_0}{2}$  and  $\text{Ca}^{2+}$  influx rate at the plasma membrane  $k_{\text{Ca}} = 0 \text{ s}^{-1}$ . 100  $\text{IP}_3$  molecules are injected in Node 1 at  $t = t_0 = 0.1 \text{ s}$ , while the number of Ca-GCaMP,  $\text{IP}_3$  and  $\text{IP}_3\text{R}$  channels in the open state are monitored in nodes 1 and 2. Molecule position was updated every 0.1 ms. Ca-GCaMP molecules are in yellow,  $\text{IP}_3$  in red and  $\text{IP}_3\text{R}$  in blue. Note that the size of molecules in the movie was increased to facilitate visualization. Speed was increased 5-fold for visualization purposes.